VYSOKÉ UČENÍ TECHNICKÉ V BRNĚ
BRNO UNIVERSITY OF TECHNOLOGY

FAKULTA STROJNÍHO INŽENÝRSTVÍ
FACULTY OF MECHANICAL ENGINEERING

LETECKÝ ÚSTAV
INSTITUTE OF AEROSPACE ENGINEERING

ANALÝZA INERČNÍHO ODLUČOVAČE ČÁSTIC NA VSTUPU VZDUCHU DO TURBOVRTULOVÉHO MOTORU

STUDY OF INERTIAL PARTICLE SEPARATOR IN A TYPICAL TURBOPROP ENGINE

DIPLOMOVÁ PRÁCE
MASTER'S THESIS

AUTOR PRÁCE — **Bc. Adam Skála**
AUTHOR

VEDOUCÍ PRÁCE — **Ing. Robert Popela, Ph.D.**
SUPERVISOR

BRNO 2019

BRNO UNIVERSITY OF TECHNOLOGY
FACULTY OF MECHANICAL ENGINEERING

Master's Thesis Assignment

Institut:	Institute of Aerospace Engineering
Student:	**Bc. Adam Skála**
Degree programm:	Mechanical Engineering
Branch:	Aircraft Design
Supervisor:	**Ing. Robert Popela, Ph.D.**
Academic year:	2018/19

As provided for by the Act No. 111/98 Coll. on higher education institutions and the BUT Study and Examination Regulations, the director of the Institute hereby assigns the following topic of Master's Thesis:

Study of Inertial Particle Separator in a typical turboprop engine

Brief description:

Ingestion of debris inside turboprop engine occurs during take-off, flight and landing. This can lead to fatal damage of the engine. Therefore, it is necessary to place a filtering device at the inlet section of the engine without significant effect on its characteristics. Inertial Particle Separator can be such a device. For reasonable filtering efficiency of broad spectra of debris, it is crucial to investigate design of this device. Study can be done experimentally, or with use of numerical simulations, which is also a cheaper option. This diploma thesis focuses on numerical analysis of IPS device.

Master's Thesis goals:

Aim of this diploma thesis is to investigate filtering capability of Inertial Particle Separator in a typical turboprop engine with use of CFD software tools. Further to perform efficiency analysis and to propose design changes for improvement of separation efficiency.

Recommended bibliography:

SEDDON, J., GOLDSMITH, E., Intake Aerodynamics, AIAA series, ISBN: 978-1-56347-361-6.

BOJDO, N., FILIPPONE, A., A Comparative Study of Helicopter Engine Particle Separators, Journal of Aircraft, Vol. 51, No. 3 (2014), pp. 1030-1042.

Students are required to submit the thesis within the deadlines stated in the schedule of the academic year 2018/19.

In Brno, 2. 11. 2018

L. S.

doc. Ing. Jaroslav Juračka, Ph.D.	doc. Ing. Jaroslav Katolický, Ph.D.
Director of the Institute	FME dean

Abstract

This thesis focuses on ingestion of foreign objects into standard turboprop engine GE H80 situated in aircraft Let L-410 Turbolet. Aim of this study is to create methodology of numerical simulation of particle movement inside the engine, which could be used during design process of Inertial Particle Separator device. Thesis consists of backward-facing step benchmark study which validates used methodology. Second part describes flow field calculation and numerical setup. The last part is dedicated to particle tracking analysis. Simulated trajectories are visually investigated, and coordinates of particle impacts at 1st rotor of a compressor are correlated to position of real observed damage.

Keywords

Inertial particle separator, Computational fluid dynamics, CFD, Particle tracking analysis, Reynolds averaged Navier-Stokes turbulence models, Compressible flow, Turboprop engine

Rozšířený abstrakt

Při startu, pojezdu či přistání letounu může dojít k nasátí cizích částic do motoru. Může se jednat například o prachové částice vyskytující se v pouštních oblastech či o větší částice asfaltu, kamení a zeminy. Při nasátí větší částice, může dojít k okamžitému poškození lopatek kompresoru či turbíny. Toto poškození může vést k nutnosti častější údržby, nebo hůře, k nevratnému poškození motoru.

Cílem této studie je ve spolupráci se společností General Electric Aviation Czech analyzovat efektivitu inerčního odlučovače částic turbovrtulového motoru GE H80 v zástavbě letounu L-410 pomocí CFD nástrojů. Analýza zahrnuje numerický výpočet proudového pole a následující simulaci nasátí cizích předmětů do motoru, tedy trasování částic od vstupu difuzoru až po první stupeň kompresoru. Dalším cílem práce je vytvoření metodologie trasování částic a posouzení její spolehlivosti porovnáním výsledků numerické simulace s reálným poškozením naměřeném na rotoru kompresoru.

Na začátku práce byla vypracována kalibrační úloha, proudění tekutiny přes schod ve dvourozměrném prostoru s následujícím trasováním částic ve vypočteném proudovém poli za pomocí softwaru Fluent. Kalibrační úloha poskytla dobré podmínky pro porovnání strukturované a nestrukturované sítě s různými hustotami buněk. Dále bylo otestováno „chování“ běžných Reynolds Averaged Navier-Stokes (RANS) modelů turbulence a mimo samotného trasování částic v závislosti na proudění také závislost zpětného ovlivnění proudění částicemi. Úloha byla validována s reálným měřením a posloužila pro ověření správnosti postupu při podobných výpočtech.

Závěrem kalibrační úlohy pro následující studii inerčního odlučovače částic bylo zanedbání ovlivnění proudění částicemi, tedy, částice jsou trasovány až po výpočtu proudového pole a toto není dále částicemi ovlivněno. Tento předpoklad je platný pro malé objemové zlomky částic ve výpočetní doméně a výrazně zjednodušuje výpočet. Také byl vybrán tzv. 2rovnicový model turbulence, Realizable $k - \varepsilon$.

Další část práce již přistupuje k problému inerčního odlučovače částic (IOČ). Tato práce zkoumá konfiguraci stojícího motoru (letounu) na dráze a nasátí cizích částic. Pro zjednodušení úlohy byly užity předpoklady jako zanedbání zavíření proudu za vrtulí, aproximace rotace prvního stupně kompresoru užitím metody několikanásobného referenčního rámce a další. Po vyčištění a zjednodušení geometrie byla vygenerována výpočetní síť s přibližně 45 miliony elementů. Nastavení výpočetní úlohy se během výpočtu měnilo z důvodu nedostatečné konvergence či divergence. Z tohoto důvodu byla také zpětně pozměněna geometrie. Konečné proudové pole bylo vypočítáno s přesností diskretizace prvního řádu a v sekci kompresoru bylo porovnáno s numerickými daty

poskytnutými GEAC. Byla shledána poměrně dobrá shoda s průměrnou deviací od 10 % po maximálně 20 %.
Po získání informace o proudění uvnitř motoru byly injektovány částice. Zájmem studie byly částice většího rozměru, schopné způsobit vážné poškození na lopatkách rotoru. Proto nebyly testovány částice menší než 300 μm. Dále bylo předpokládáno, že částice se po dopadu nerozpadá a částice je sférická bez rotace. Velký význam při pohybu částice v proudu kapaliny má její velikost a hustota. Při vytváření finální geometrie domény byla zanedbána krycí mřížka před vstupem do kompresoru omezující vstup částic větších než 3 mm. Tak byla určena horní hranice pro testované částice, kterými nakonec byly 0.3, 0.5, 1, 1.5, 2, 2.5 mm sféry s hustotami 1800 a 2600 $kg \cdot m^{-3}$. Velkému zájmu byl podroben součinitel restituce, definující ztrátu energie částice při srážce s druhým tělesem. Nejprve byly testovány konstantní hodnoty od 1 po 0.6 pro normálovou i tangenciální složku součinitele restituce. Dále byly testovány polynomická vyjádření tohoto součinitele. Částice o dané velikosti a hustotě byly vypuštěny do domény s rychlostí 1, 5, 10, 20 a 30 $m \cdot s^{-1}$ vždy v počtu přibližně 200, a poté analyzovány dohromady. Takto byly vpuštěny všechny velikosti částic. Ve výsledku tak vzniklo 420 případů částic s různým nastavením zmíněných veličin. Pomocí Spearmanova Rho testu byla vyhodnocena míra korelace mezi simulovanými daty a skutečně pozorovaným poškozením. Tato data, pocházející z měření provedeném na 4 rotorech, laskavě poskytla společnost GEAC.

Největší míru korelace, až 75 %, zaznamenaly konfigurace s menšími průměry částic do 1 mm, a to pro obě hustoty částic. Se zvětšující se velikostí částic míra korelace klesala. Lze tak usuzovat, že poškození motoru způsobují zejména tyto částice, a to se spíše s nižší hustotou. Podrobnější zkoumání citlivosti na rychlost vpuštění do motoru ukázala, že nejvyšší míra korelace pro částice 0.3 a 1 mm je pravděpodobně kolem 10 $m \cdot s^{-1}$.

Vizuální prohlídka trajektorie částic přinesla zjištění, že trajektorie se většinou dělí na dvě části. Jedna skupina částic vletí do spodní části motoru s IOČ a zde jsou buď lapeny, nebo se odrazí zpět. Druhá skupina IOČ mine a narazí do zdi ustalovací komory nad odlučovačem. Po odrazu zpět do hlavního proudu jsou tímto strhnuty a jsou přímo nasáty do kompresoru, nebo častěji, doputují do horní části ustalovací komory a odsud vletí do kompresoru.

Byla také prozkoumána varianta s otevřenou klapkou odlučovače, která je mimo námrazové podmínky zavřená. Proudové pole nebylo pro otevřenou klapku přepočítáno, její plocha byla pouze přenastavena na lapení částic. Otevření této klapky i v dalších fázích provozu, zejména vzletu a pojezdu, by mohlo vést k eliminování významného počtu částic, které jsou jinak odraženy zpět do proudu a následně nasáty do kompresoru.

Přínos této práce je zejména ve vyvinutí metodologie numerického trasování částic a posouzení jeho spolehlivosti. Poměrně vysoká míra korelace některých nastavení, a to i přes množství zjednodušujících předpokladů ukázala, že tato metoda může posloužit k pochopení pohybu částic uvnitř turbovrtulového motoru a ušetření nákladů na vývoj a návrh efektivnějšího odlučovače částic. Kromě zvýšení bezpečnosti toto může vést k dalšímu snížení nákladů na opravy, servis a méně časté prohlídky.

Klíčová slova

Inerční odlučovač částic, Výpočetní dynamika tekutin, CFD, Trasování částic, RANS modely turbulence, Stlačitelné proudění, Turbovrtulový motor

Bibliographic citation

SKÁLA, Adam. *Study of Inertial Particle Separator in a Typical Turboprop engine*. Brno, 2019. Available at: https://www.vutbr.cz/studenti/zav-prace/detail/117606. Master's thesis. Brno University of Technology, Faculty of Mechanical Engineering, Institute of Aerospace Engineering. Supervisor Robert Popela.

Bibliografická citace

SKÁLA, Adam. *Analýza inerčního odlučovače částic na vstupu vzduchu do turbovrtulového motoru*. Brno, 2019. Dostupné také z: https://www.vutbr.cz/studenti/zav-prace/detail/117606. Diplomová práce. Vysoké učení technické v Brně, Fakulta strojního inženýrství, Letecký ústav. Vedoucí práce Robert Popela.

Declaration of Authorship

I hereby declare that I have authored this thesis independently, that I have not used other than the declared sources, and that I have explicitly marked all material which has been quoted either literally or by content from the used sources.

Brno, May 23rd 2019 Adam Skála

Acknowledgement

I would like to express my gratitude to Robert Popela, my supervisor at Brno University of Technology, for his guidance and helpful discussions. Also, I would like to thank to Luca Lombardi, my supervisor at General Electric Aviation Czech, who gave me opportunity to work on this master's thesis and provided me with the data and valuable answers. Finally, I would like to thank to my family for never ending support throughout the studies.

'I love deadlines. I love the whooshing noise they make as they go by.'
-Douglas Adams

Table of Contents

1 Introduction

During take-off, landing or taxiing on the ground, aircraft engine can ingest foreign objects. The character of objects can vary from dust or sand to larger pieces of asphalt or concrete runway. When large particle (from 0.3 to 3 mm, as defined in this thesis) is ingested, damage may occur. Compressor blades and turbine stages are critical parts that are most prone to damage caused by ingestion of foreign objects. The damage of blades leads to loss of efficiency of the engine and more frequent service intervals.

The inertial particle separator (IPS) is a device which is often installed in turboprop engines and is designed to protect engine from ingestion of particles to compressor section. The aim of this thesis is to analyse effectiveness of such device installed in turboprop engine GE H80 situated within aircraft Let L-410 Turbolet using CFD tools. The analysis includes numerical computation of flow field and particle tracking through engine installation. The presented study is also aiming to investigate possible methodology of particle tracking and to review its reliability with statistical comparison of simulated results and real observed damage at the first rotor stage of compressor.

This thesis was produced in collaboration with the General Electric Aviation Czech company and is divided into three parts. The first part deals with the benchmark case of backward-facing step, verification of used method and it introduces theory needed for simulating the flow field and particle tracking. The second part describes assumptions made in order to calculate the flow field, the calculation setup itself and validation of the model with provided data. The last part of the thesis investigates the influence of various parameters on particle movement. The way the ingested particles are behaving is evaluated visually and possible method of their numerical tracking is proposed in chapter 4.

2 Benchmark study

2.1 Introduction

To practise methodology and gain experience in particle tracking analysis using Fluent solver, well-known benchmark study of flow over 2D backward-facing step (BFS) was chosen. Another aim was to investigate behaviour of various turbulent models and support its choice for further study. To validate results, experimental study of Fessler and Eaton (1999) was used. Numerical study of Greifzu et al. (2016) was utilized while setting up the solver. BFS benchmark study also aims to investigate behaviour of unstructured mesh in comparison with structured one.

2.2 Method

2.2.1 Domain & Boundary Conditions

Geometry of BFS is shown in Figure 2.1. Dimensions of a channel with the step are given by previously mentioned studies. To let the flow fully develop, lengths of 130H in front and 50H behind the step were assumed as sufficiently long.

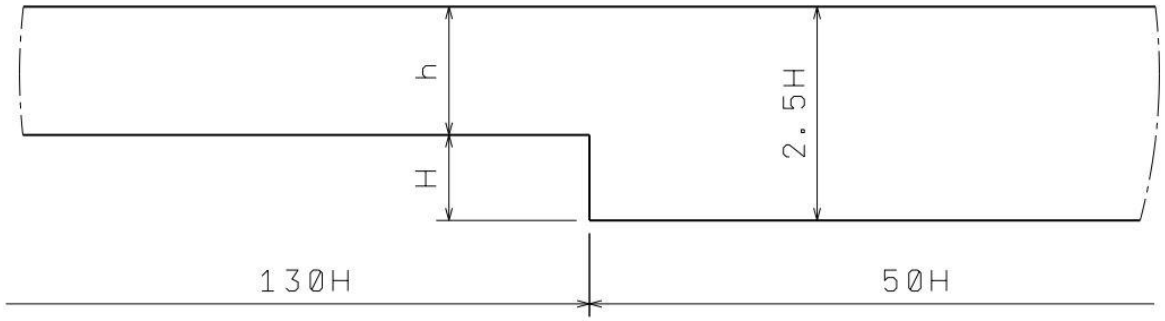

Figure 2.1 – Geometry of BFS

Flow properties were determined based on desired Reynolds numbers and they are listed in Table 2.1. Velocity-inlet boundary condition and pressure-outlet with zero-gauge pressure were applied at the beginning and at the end of the channel respectively. No-slip wall condition was assigned to walls. Operational pressure was kept default – 101 325 Pa.

Table 2.1 – Flow properties

Channel flow:		**BFS flow:**	
Channel width h	40 mm	Step height H	26.7 mm
		Expansion ratio	5 : 3
Inlet velocity U	10.43 m·s^{-1}		
Centreline velocity U_0	11.55 m·s^{-1}		
$Re_h = \frac{U \cdot h/2}{\upsilon}$	13 800	$Re_H = \frac{U \cdot H}{\upsilon}$	18 400
Fluid	Air, 20°C		

2.2.2 Mesh

Due to complexity of an IPS geometry, an unstructured mesh is utilized later in this study. Therefore, it is desired to investigate its behaviour compared to experimental data and results obtained with structured mesh. Near wall resolution was made to satisfy $y^+ \approx 1$ for both types of grids. To satisfy higher values of y^+ for this particular case of BFS, mesh would be too coarse.

To investigate mesh independency, x-, y-velocities were observed at 2, 5, 7, 9 and 12 step heights behind the step for several resolutions which are listed in Table 2.2. Velocities at x/H=2 position are shown in Figure 2.2 and the rest of velocity profiles is shown in Appendix A. As seen in Figure 2.2, main differences were observed in y-velocity directly behind the step, in recirculation area, approximately at y/H=0.44.

Table 2.2 – Overview of mesh resolutions, bolded ones give independent results for $Re_h = 13\,800$

	Nodes:	**Cells:**	**Difference:**
Unstructured (Tet)	37k	52k	77 %
	87k	140k	5.3 %
	167k	**283k**	**1.1 %**
	282k	480k	
Structured (Hex)	35k	35k	16 %
	78k	**77k**	**0,9 %**
	153k	152k	0,7 %
	363k	360k	

Criterion of maximal difference around 1 % after refinement was enough to consider results as mesh independent. No significant differences were observed in x-velocities at all positions as seen in left part of Figure 2.2.

It can be seen, reaching mesh independency with unstructured mesh were somewhat more difficult. Bolded resolutions were picked for further particle tracking analysis according to differences shown in Table 2.2.

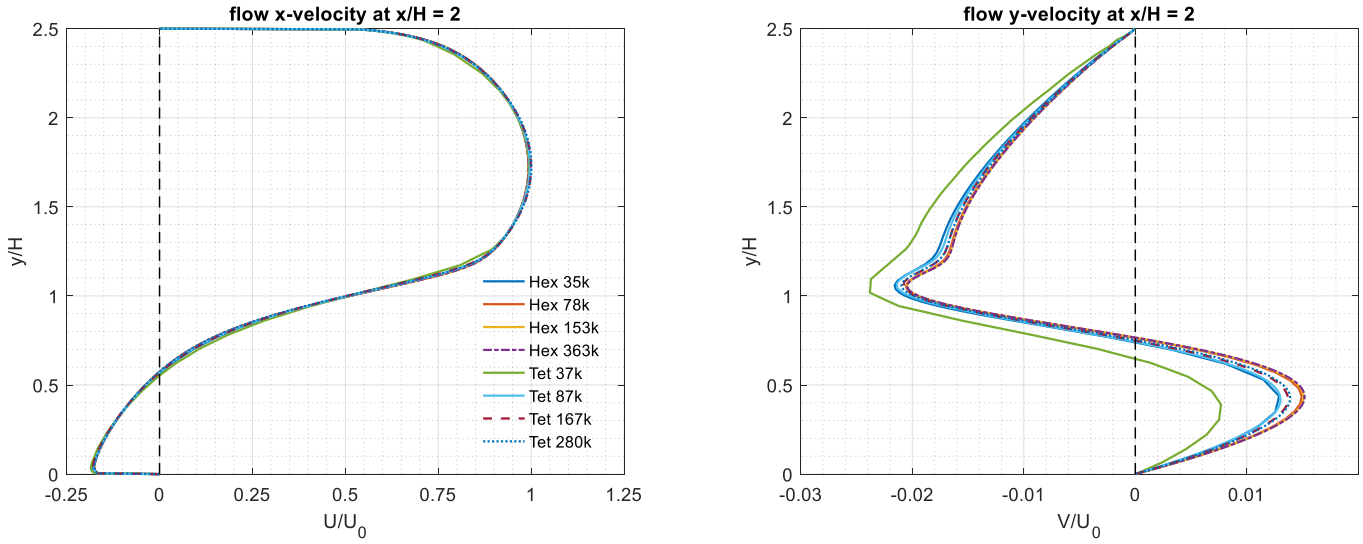

Figure 2.2 – Mesh independency, x- and y-direction velocities at x/H=2, velocities normalized by centerline velocity U_0

2.2.3 Numerical Setup

Important question while setting up a case is choice of a turbulence model. For complex industrial use, Reynolds Averaged Navier-Stokes (RANS) models are commonly utilized. These models are known for their relatively low computational demand, sufficient level of accuracy and robustness.

Most common models are two-equation RANS models, $k-\varepsilon$ (SKE) and $k-\omega$. These models enclose Navier-Stokes problem with 2 additional transport equations, where k is a kinetic energy per unit mass of turbulent fluctuations. Reynold stresses are modelled by variable called eddy viscosity.

$k-\varepsilon$ *turbulence models*

Second transport equation solves for ε, rate of dissipation of kinetic energy, which describes the scale of a turbulence. This model is reasonably accurate in free shear flows and flows with small pressure gradients. Near wall treatment is done by wall functions which analytically solve fluid behaviour in viscous sub-layer of boundary layer. It is well known that $k-\varepsilon$ model performs weakly in near wall regions and in regions with great adverse pressure gradients where separation is delayed, and reattachment is underpredicted.

Realizable $k-\varepsilon$ (RKE) contains improved ε-equation and new eddy-viscosity formulation. It predicts boundary layer in adverse pressure gradient regions more satisfactory, also it performs more accurately in recirculation areas.

$k-\omega$ *turbulence models*

For turbulence scale determination, specific turbulence dissipation rate ω is used. This transport equation can be integrated through viscous sub-layer without any additional term and thus, this model is able to predict near-wall behaviour (e.g. in adverse pressure gradient flows) more accurately relative to $k-\varepsilon$ model. Because it does not use any wall function, it is necessary to refine mesh and place first cell into viscous sub-layer. That is described by y^+ value, which should be around 1. Draw-back of standard $k-\omega$ model is its poor performance when used in free shear flow. Therefore, it is not recommended to use in ANSYS Fluent software.

To enhance poor behaviour outside shear layer, combination of $k-\varepsilon$ and $k-\omega$ models was created. Most famous model is Menter's shear stress transport (SST) turbulence model. It uses Blending function to switch between those two models depending on wall distance. That means in free shear flow, $k-\varepsilon$ is used and in viscous near-wall regions, $k-\omega$ is utilized. Advantage of SST model is flow separation and reattachment prediction, on the other hand, turbulence levels in stagnation regions or regions with high acceleration can be overpredicted.

Overview of turbulence models was derived from (ANSYS Fluent Theory Guide [AFTG], 2013, sections 4.1 – 4.6), (ANSYS Fluent User's Guide [AFUG], 2013, sections 12.2 – 12.6), (SST k-omega model, 2011), (K-epsilon models, 2011) and (Wasserman, 2011).

All above mentioned turbulence models were tested and compared against experimental data by Fessler and Eaton (1999) to choose most suitable one for IPS study.

Numerical setup for each turbulence model is listed in Table 2.3. Pressure-Velocity coupled solver was used for all simulations. Due to fine near wall resolution, especially for $k-\varepsilon$ models, Scalable wall function was paired with SKE and RKE models, ensuring shift of the first cell of the grid to log-law region where $y^+ \geq 11.2$. When y^+ is higher than this limit, scalable wall function behaves in same manner as standard wall function, (AFUG, 2013, section 4.14.3). For scalable wall function is therefore established variable $y^* = max(11.2,\ y^+)$.

Table 2.3 – Numerical setup for various turbulence models

	SKE – RKE – SST turbulence models
Scheme	SIMPLE
Gradient	Least Square Cell Based
Pressure	2nd Order
Momentum	2nd Order Upwind
Turbulent Kinetic Energy	2nd Order Upwind
Turbulent Dissipation Rate	2nd Order Upwind
Under-Relaxation Factors	Pressure – 0.3 Momentum – 0.7 Turbulence – 0.8

Problem with convergence occurred while running the SST simulation, under-relaxation factors had to be lowered for pressure – 0.5, momentum – 0.5 and turbulence – 0.7.

2.2.4 Convergence

To control level of convergence, several points throughout the domain (especially in separation area and in channel behind the step) were created. Velocities in x- and y-direction were monitored and after reaching steady state in all points, solution was assumed as converged. Scaled residuals were used as a helping criterion of convergence but reached recommended values long before velocities got steady.

2.2.5 Particle tracking analysis

In numerical simulations, behaviour of dispersed phase (solid particles in this study) is influenced by continuous fluid phase. Trajectory of particle is solved by integrating its force balance in a Lagrangian reference frame. Force balance can be written as

$$\frac{d\overrightarrow{u_p}}{dt} = F_D\left(\vec{u} - \overrightarrow{u_p}\right) + \frac{\vec{g}(\rho_p - \rho)}{\rho_p} + \vec{F} \tag{2.1}$$

where $\frac{d\overrightarrow{u_p}}{dt}$ is particle inertia term, $F_D\left(\vec{u} - \overrightarrow{u_p}\right)$ is drag force term, $\frac{\vec{g}(\rho_p - \rho)}{\rho_p}$ is gravity term and $\vec{F}$ is additional acceleration, all terms are for unit particle mass. Drag force is obtained as

$$F_D = \frac{18\mu}{\rho_p d_p^2}\frac{c_D Re_p}{24} \tag{2.2}$$

where μ is molecular viscosity of fluid, ρ_p is particle density and d_p is particle diameter. Relative (particle) Reynolds number can be calculated

$$Re_p = \frac{\rho d_p |\overrightarrow{u_p} - \vec{u}|}{\mu} \tag{2.3}$$

where ρ is fluid density, $\vec{u}$ and $\overrightarrow{u_p}$ is fluid phase and particle velocity respectively. Gravitational acceleration is zero by default in Fluent and adding this term must be turned on.

Significant simplification used in this study is assumption of spherical particles. Therefore, spherical drag law is used

$$c_D = a_1 + \frac{a_2}{Re_p} + \frac{a_3}{Re_p^2} \tag{2.4}$$

where a_1, a_2 and a_3 are constants for several ranges of Re_p given by Morsi and Alexander (1972).

As said in the beginning of this paragraph, particles or generally dispersed phase is influenced by fluid phase. The extend of coupling between dispersed and flow phase is shown in Figure 2.3 and is determined by volume fraction of particles – α_P. For low volume fraction of particles $\alpha_P < 10^{-6}$, one-way coupling is used. That means, movement of particles is determined by the drag and optionally buoyancy and gravity. However, effect of particles on flow phase is negligible. For $10^{-6} < \alpha_P < 10^{-3}$, two-way coupling is used. This method accounts influence of particles on flow structure. The influence can be either increased dissipation rate of turbulence energy or its increased production in flow. This is determined by the second coordinate, τ_p/τ_e or τ_p/τ_K, where τ_p is particle response time, τ_K is Kolmogorov time scale and τ_e is large eddy turnover time or representative flow timescale. For even higher particles loading, interaction between particles must be taken in account, therefore four-way coupling is introduced. More information about particle theory is provided in chapter 4.

Overview of particle tracking theory was derived from (Greifzu et al., 2016), (Elghobashi, 1994). Equations were taken from (AFTG, sections 16.2 – 16.3).

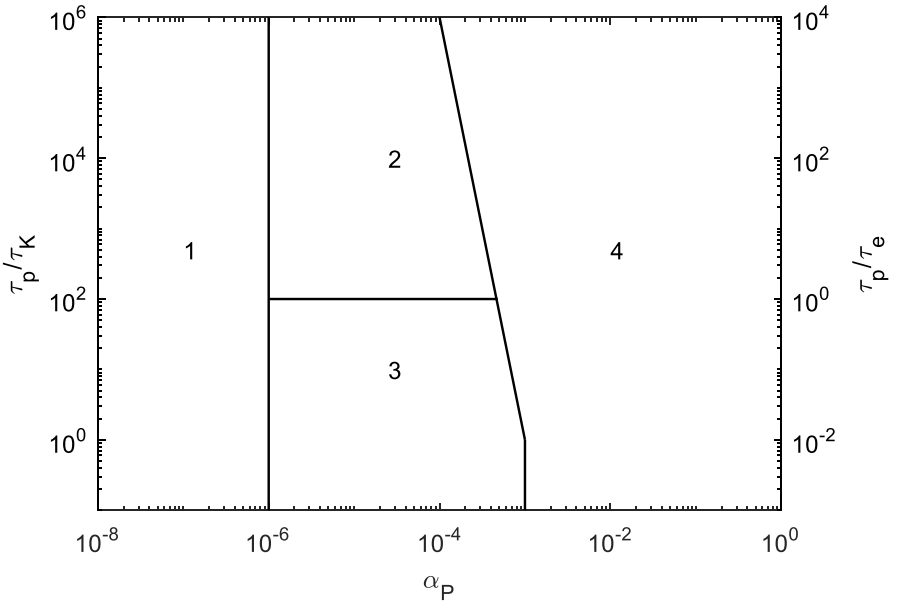

Figure 2.3 – Dispersed and flow phase interaction diagram, 1 – one-way coupling, 2 – particles enhance production, 3 – particles enhance dissipation, 4 – four-way coupling, adapted from (Elghobashi, 1994, p.310)

Copper particles of diameter 70 μm were used in experimental study of Fessler and Eaton (1999). Same particles, in quantity of 30, were injected at the beginning of studied BFS channel. All particle

parameters used in Fluent are listed in Table 2.4. Volume fraction of 30 copper particles injected in channel is well bellow $\alpha_P < 10^{-6}$, therefore one-way coupling was investigated mainly.

Table 2.4 – Properties of injected particles

Particles:	
Particle density ρ_p	8800 kg·m^{-3}
Particle diameter d_p	70 μm
Initial velocity	10.43 m·s^{-1}

2.2.6 Investigated cases

Table 2.5 shows description of investigated cases which can be seen in Results and Discussion.

Table 2.5 – Case description

Case name:	**Turbulence model:**	**Mesh:**	**Particle coupling:**	**Wall function:**
Hex k-eps	Standard $k-\varepsilon$	Hex 78k	One-way	Scalable
Tet k-eps	Standard $k-\varepsilon$	Tet 167k	One-way	Scalable
Tet rk-eps	Realizable $k-\varepsilon$	Tet 167k	One-way	Scalable
Tet coupled	Standard $k-\varepsilon$	Tet 167k	Two-way	Scalable
Tet SST	SST $k-\omega$	Tet 167k	One-way	-

2.3 Results & Discussion

Study of Fessler and Eaton (1999) provided experimental data, specifically x-direction velocity profiles of fluid phase and velocity profiles of copper particles in same regions. Those were used to validate numerical results obtained with various turbulence models, which were also compared against each other. Study paper by Greifzu et al. (2016) also provided comparison and validation of particle tracking in Fluent solver. However, these are not shown in figures bellow. Flow and particles velocity profiles at x/H=2, 7 and 12 are shown. Remaining sections can be found in Appendix B. All velocities are normalized by centreline velocity U_0.

Flow phase profiles are shown on a left side. It can be seen, free-shear flow is predicted well by all turbulence models. In recirculation area, velocities are overpredicted near the wall, SST model is closest to real data, but its performance is not substantially better than rest.

In sections further downstream, flow velocity is predicted in good agreement by SST and by RKE models. Only minor differences can be seen between those two, where RKE seems more accurate. With no difference whether structured or unstructured mesh, SKE model underpredicts flow velocity further downstream. As expected, with low particle loading, two-way coupling has no influence on flow phase and profiles are spot on with those non-coupled ones.

Fluent solver does not predict presence of particles in recirculation area behind the step, which is in good agreement with measured data by Fessler and Eaton (1999). However, the lateral spreading is weaker towards the bottom wall at all sections. The shape of velocity profiles seems reasonable and it does not suggest 'block profile' distribution mentioned by Greifzu et al. (2016). Magnitude of particle velocity is close to experiment directly behind the step, whereas at x/H=12, velocity of particles is ≈15 % higher than experiment. As the flow does lose some of its momentum due to widening of the channel, particles do not slow down as fast. This overprediction of momentum could be caused by the lack of lateral spreading or two-dimensional nature of the numerical study. As expected, no influence of two-way coupling was found when compared to one-way coupled particles. Despite obvious differences in flow phase predictions by different turbulence models, the particle predictions seem similar with only minor magnitude differences.

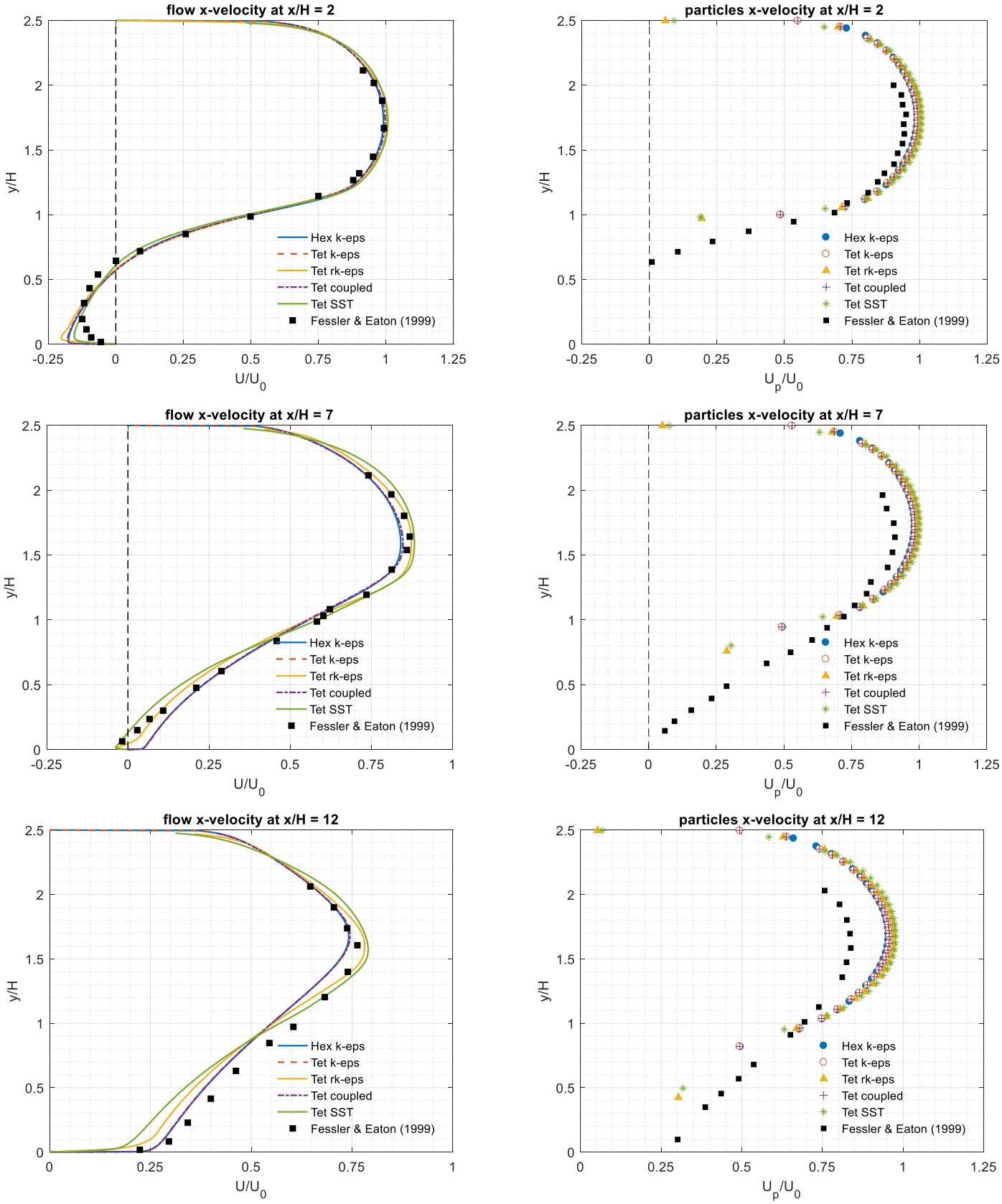

Figure 2.4 - Flow and discrete phase velocity profiles at x/H=2, 7, 12; velocities are normalized by centreline velocity U_0

2.4 Conclusion for IPS study

Benchmark fulfilled its aim to investigate theory and practical way of particle tracking analysis in commercial software such as Fluent for more complex three-dimensional problems. Furthermore, it showed that flow phase can be predicted by various turbulence models with a reasonable level of accuracy. For further study, Realizable $k-\varepsilon$ and SST $k-\omega$ turbulence models were considered as most suitable. From all tested models, RKE model was the most accurate, while easier to converge than SST model. Scalable wall function was utilized with $k-\varepsilon$ models and is suitable for scope of IPS study.

It was shown, that unstructured mesh performs as good as structured one when sufficiently refined. No more hints regarding mesh generation in IPS geometry could not be taken from BFS study for its two-dimensional nature and much lower velocities of flow.

The particle tracking analysis was focused mainly on one-way coupling with flow phase. The analysis showed, that for low fraction volumes of dispersed phase, two-way coupling does not bring any improvement.

3 Inertial Particle Separator – Flow field

3.1 Introduction & Assumptions

To inject and track particles through any domain, obtaining accurate flow field is important step of a process. At the beginning of IPS flow field investigation, several assumptions were used to simplify the problem. Major assumptions are stated in this paragraph, others are introduced and motivated further in the text.

External geometry of wing and plane fuselage was neglected. Effect of this missing geometry should be insignificant due to the fact, that the plane and engine are stationary in a reference to the ground. Therefore, the main and only effect on flow entering the engine intake is caused by rotation of a propeller and shape of an intake nacelle. Further assumptions regarding geometry are stated in section Geometry.

Rotation of a rotor can be simulated in a time, using e.g. moving mesh approach. That would lead to enormous increase of a computational time and thus, stationary method which approximate the angular movement of a rotor was applied. This approach is approximation, but widely used in industry and thus is suitable for scope of this study.

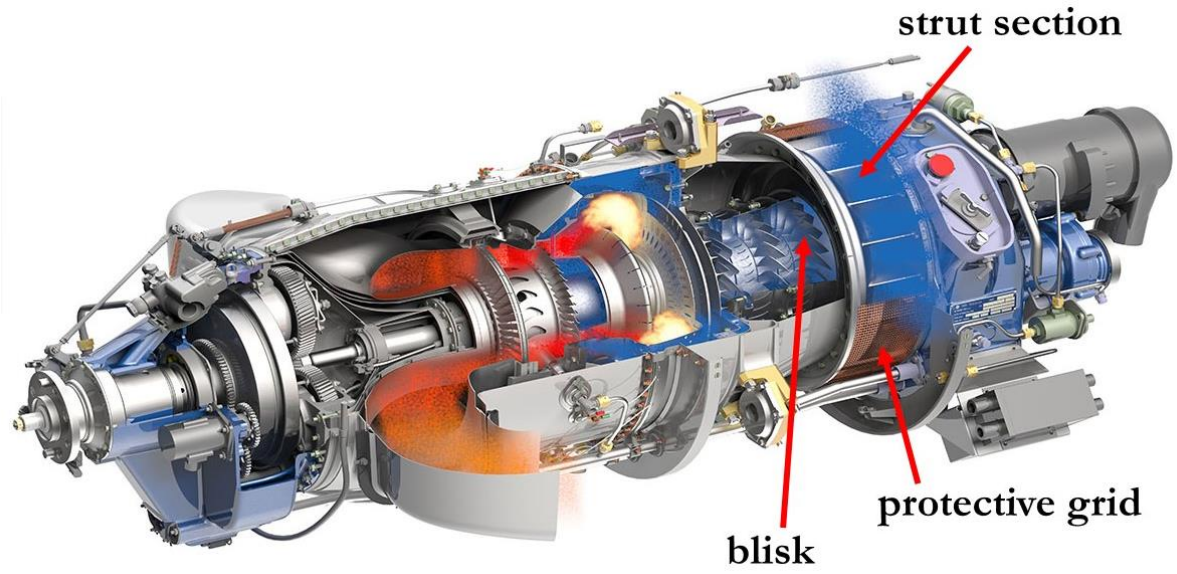

Figure 3.1 – Engine GE H80 with used terminology, adopted from ("Motory H-Series", 2016)

3.2 Geometry

Investigated geometry comes from turboprop engine GE H80 with intake subassembly mounted on aircraft L-410. The geometry was simplified, inner tubes and other small devices inside stilling chamber were removed. Protective metal grid (Figure 3.1) in front of strut section, which is preventing foreign objects from spreading further down the engine, was also removed. It was assumed, the effect of a grid on pressure filed is negligible. Filtering ability of the metal grid is implemented by excluding particles bigger than its resolution. Details which could affect the particle paths were kept. Model includes first rotor of a compressor – blisk. Figure 3.2 shows original and simplified geometry.

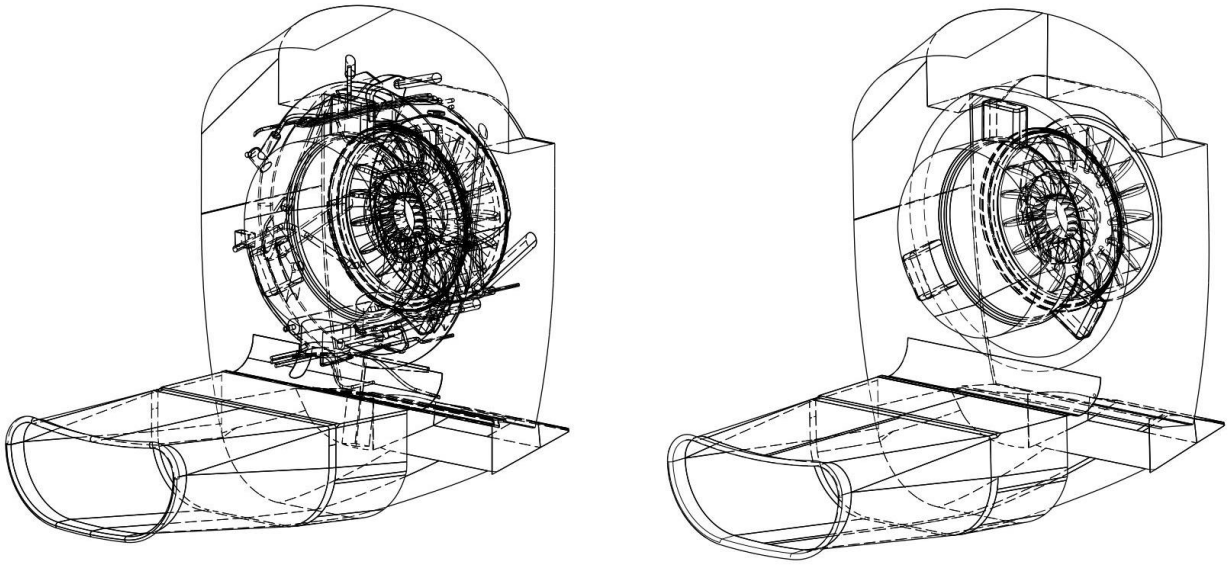

Figure 3.2 – Original and simplified geometry of the IPS from left to right respectively

The domain was extended by 'inlet box' showed in Figure 3.3. This was done to include inlet velocity parameters which are strongly affected by rotation of a propeller. Furthermore, it gives more options to inject particles from. The box reaches ca 150 mm in front of engine. This was done to utilize provided inlet data by GEAC. These data were extracted from simulation involving propeller and thus its effect on flow. 'Inlet box' had to be enlarged during calculation process because of problems with convergence, the change is illustrated in Figure 3.3.

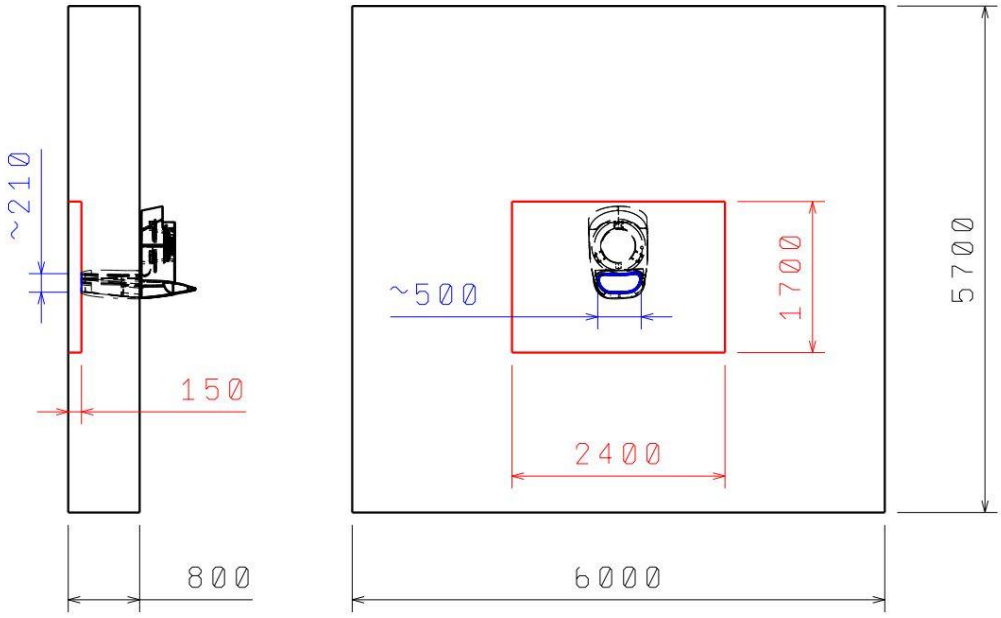

Figure 3.3 – Geometry of IPS with 'inlet box', red lines represent initial design, black lines illustrate enlarged domain, engine intake dimensions are blue

Due to increased length of the 'inlet box' and therefore including the external region of engine intake, artificial cover diffuser had to be modelled. It was designed to approximate real engine cover, especially the nacelle region. External cover of the engine intake is shown in Figure 3.5 in blue colour.

3.3 Domain & Boundary conditions

Domain was divided into two zones. Stationary zone – ('inlet box', intake and stilling chamber geometry) and rotating zone containing rotor region. To include effect of rotation of a compressor rotor and keep the state of simulation steady, multiple frame reference (MFR) approach had to be utilized. More about MFR in section Multiple reference model.

Boundary conditions applied at the 'inlet box' are shown in Figure 3.4. Blue surface marks inlet into the domain. Green side walls of the 'intake box' were initially considered as free-slip walls to influence flow as little as possible. During calculation, these were changed to inlet to prevent undesired reversed flow in corners of the 'inlet box'. Grey colour marks no-slip walls.

Flow exits domain at two outlets, compressor outlet and 'inlet box' outlet marked with red colour that are showed in Figure 3.5 and Figure 3.4 respectively. Initially, there was also oil cooler outlet, shown in Figure 3.5. This was neglected during calculation process to simplify setup and convergence. Besides, the parameters of flow through oil cooler were unknown. Yellow surface in Figure 3.5 shows where IPS flap is located. The IPS flap is being opened only during icing conditions, (Airplane Flight manual for the L 410 UVP - E20, 1998). Ingestion of debris (ice) during those conditions was not scope of this study and therefore the simulation was run with IPS flap closed.

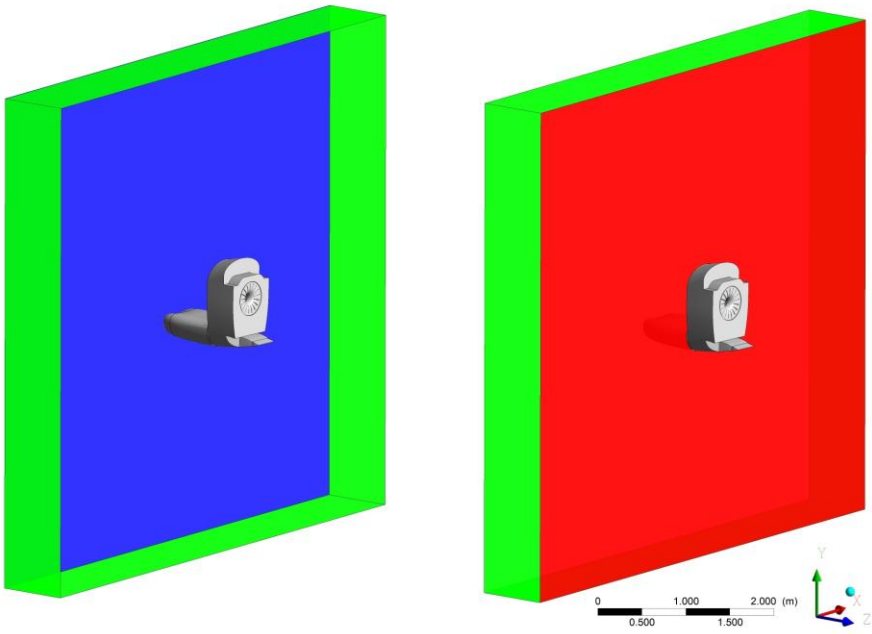

Figure 3.4 – Surfaces distinguished by colour, blue – inlet, red – outlet, green – inlet box wall, grey – wall

Figure 3.6 shows rotating cell zone and boundary conditions applied at its surfaces. Original geometry of a domain ends directly behind the rotor, further downstream would be stator stage. Presence of an outlet at proximity of a rotor caused problems during calculation. This was solved by prolonging the canal by 200 mm and shifting the outlet further away from rotor as seen in Figure 3.6. Table 3.1 and Table 3.2 show specific boundary conditions types for each zone and their parameters set in Fluent software.

In a cell zone with rotor, Frame motion was enabled with rotational velocity 36 660 revolutions per minute, which is the reference value of full thrust of GE H80 engine. Since the frame reference of the cell zone is rotating, setting up the rotor wall as stationary in that reference frame means, the rotor is moving with the same velocity. Consequently, the shroud wall was set as stationary in an absolute reference frame.

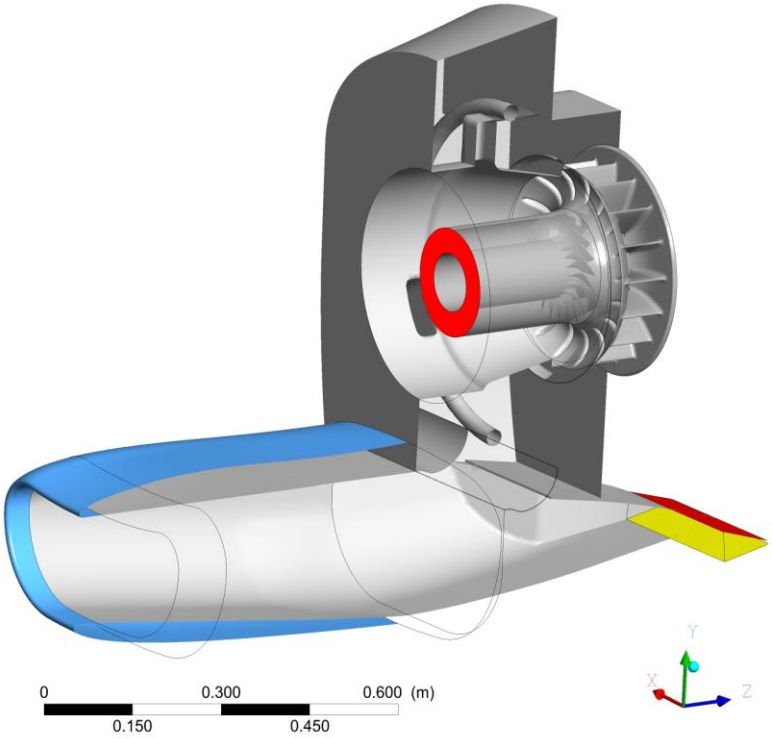

Figure 3.5 – Cross-section of IPS domain, blue surface – artificial external cover wall, red surface – compressor outlet, red surface in right bottom corner – oil cooler outlet, yellow surface – IPS flap, grey surface – wall

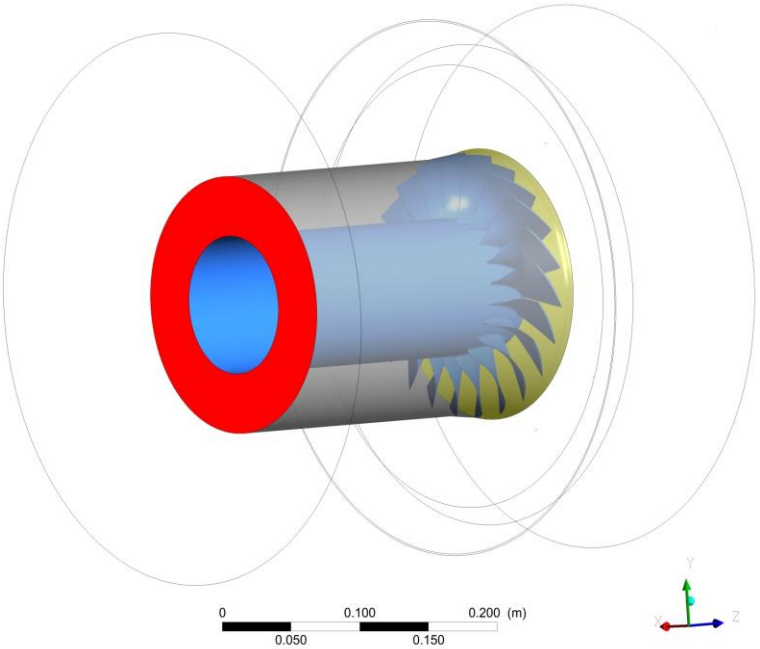

Figure 3.6 – Prolonged canal and shifted outlet, blue surface – rotor with angular velocity, yellow – interface connecting stationary and rotating zones, grey – stationary shroud wall

Data about flow behaviour behind the propeller were provided by GEAC. Data came from 'frozen rotor' simulation, meaning velocities were uneven. Thus, all three components of velocities were averaged (from region directly in front of engine intake) and applied at inlet surface as axial, tangential and radial components. Due to missing external geometry of engine and significant tangential component in region where engine cover would be, those inlet conditions created non-real situation and consequently caused reversed flow at outlet surface of 'inlet box'. This problem was solved by using only averaged z- and x-components which were applied to substitute for propeller axial and tangential components of flow.

During the calculation, presence of the x-component of a velocity induced significant recirculation zone inside the diffusor, which was expected. However, that recirculation possibly caused decrease of mass flow rate through diffuser region and lack of air delivery to compressor. To maintain target mass flow rate set on compressor outlet, flow behind the rotor had to be accelerated to super-sonic values. Solution did not reach convergence.

Final solution was obtained only with normal component of velocity at the inlet only. Parameters of final setup are stated in Table 3.1.

Table 3.1 – Applied boundary conditions and flow parameters at stationary cell zone

Stationary zone	**Boundary condition**	**Parameters**
Inlet	Velocity-inlet	x-component = 0 y-component = 0 z-component = 36 $m \cdot s^{-1}$
Intake box outlet	Pressure-outlet	Gauge pressure = 100 000 Pa
Intake box wall	Free-slip wall	Shear stress = 0
Wall	No-slip wall	-

GEAC also provided data with flow parameters behind the rotor blade. Thus, Pressure-outlet with gauge pressure and target mass flow rate was applied at compressor outlet zone. However, gauge pressure is computed by solver when flow is locally supersonic. Radial equilibrium pressure distribution option was enabled, meaning entered gauge pressure is applied at smallest radius and the rest is computed by solver assuming no radial velocity.

Table 3.2 - Applied boundary conditions and flow parameters at rotational cell zone

Rotational zone	**Boundary condition**	**Parameters**
Compressor outlet	Pressure outlet	Gauge pressure = 100 000 Pa Targeted mass flow rate = 3.93 $kg \cdot s^{-1}$ Radial equilibrium pressure distribution
Rotor	No-slip wall	Stationary wall relative to adjacent cell zone
Shroud	No-slip wall	Stationary in an absolute reference frame

3.4 Mesh

Mesh was created with ICEM CFD meshing tool. Unstructured tetrahedron patch-conforming mesh was chosen due to highly complex geometry of engine intake, especially thin blades of compressor and struts. To ensure quality criterion, these regions needed to be significantly refined as seen in Figure 3.8. Octree meshing algorithm was used for grid generation. Prism layers were generated after volume mesh was done. Surface and volume mesh are showed in Figure 3.7. To

capture boundary layer (BL) development, five layers of prism elements were generated at all internal surfaces with several exceptions (mainly surfaces, where flow separation was expected). Three layers were considered as enough at rotor and shroud surfaces for already fine mesh surrounding complex geometry of blades as seen in Figure 3.8. Adding more prism layers also caused difficulties to satisfy desired quality of elements.

Height of the first prism element was chosen to satisfy recommended values of $y^+ \geq 11.2$. Resolved viscous subregion of BL was not required for scope of this study and would dramatically increase computational time. Figure 3.9 shows overall y^* values throughout the domain. Final grid contained 45 million elements with maximum aspect ratio of 55 and minimal orthogonal quality of 0.037. More figures of created mesh are showed in Appendix C.

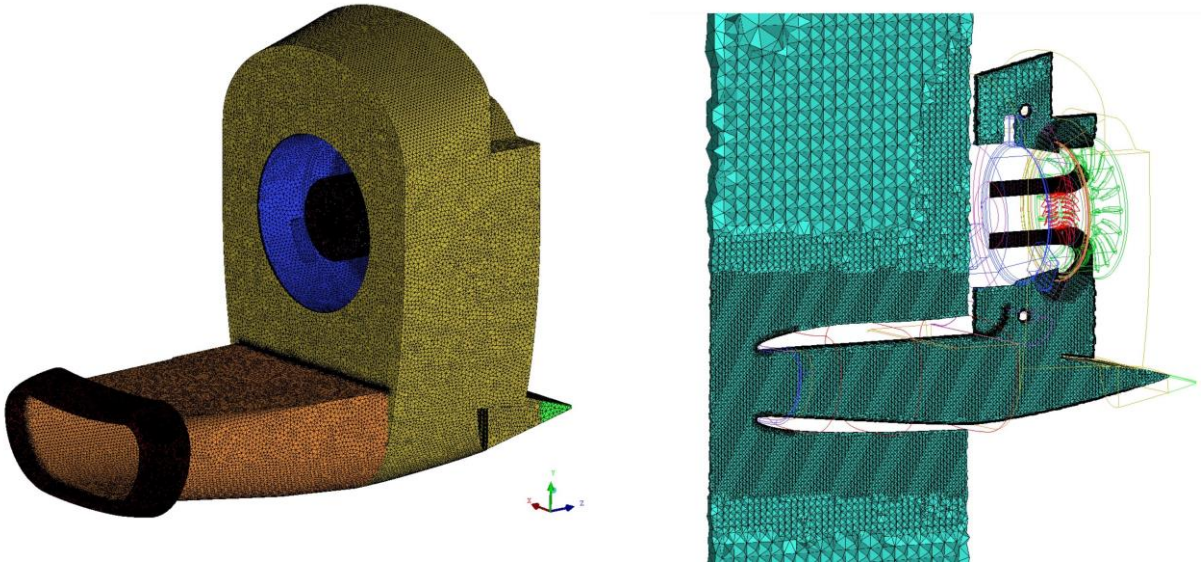

Figure 3.7 – Left side- surface mesh without external cover surface, right side – volume mesh visualized by cut plane, gradual refinement towards compressor stage where increase of velocity was expected

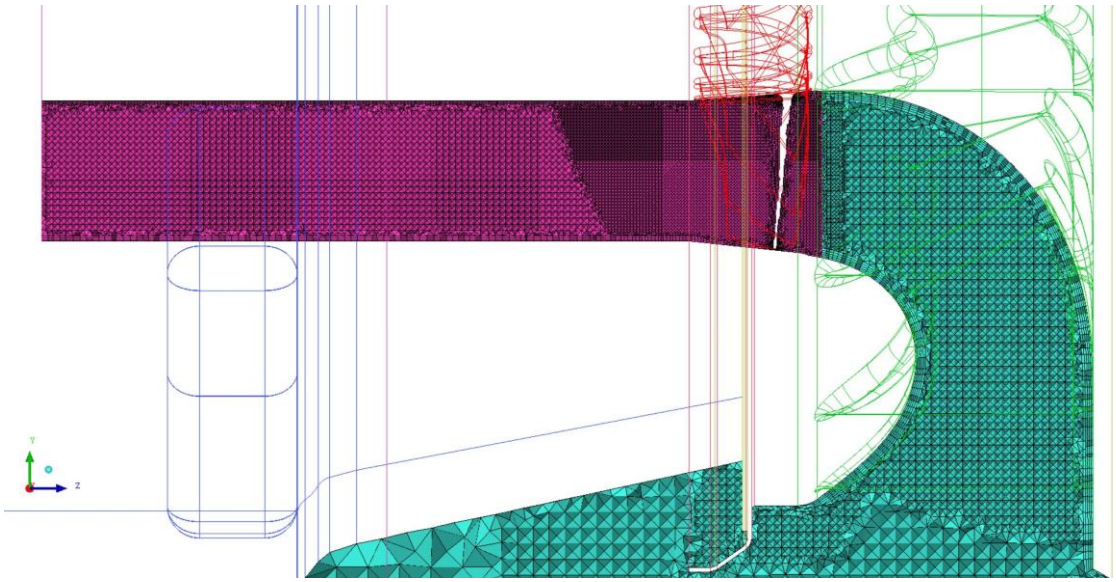

Figure 3.8 – Detailed view on refined rotor region,
the gap in pink region is caused by presence of a blade

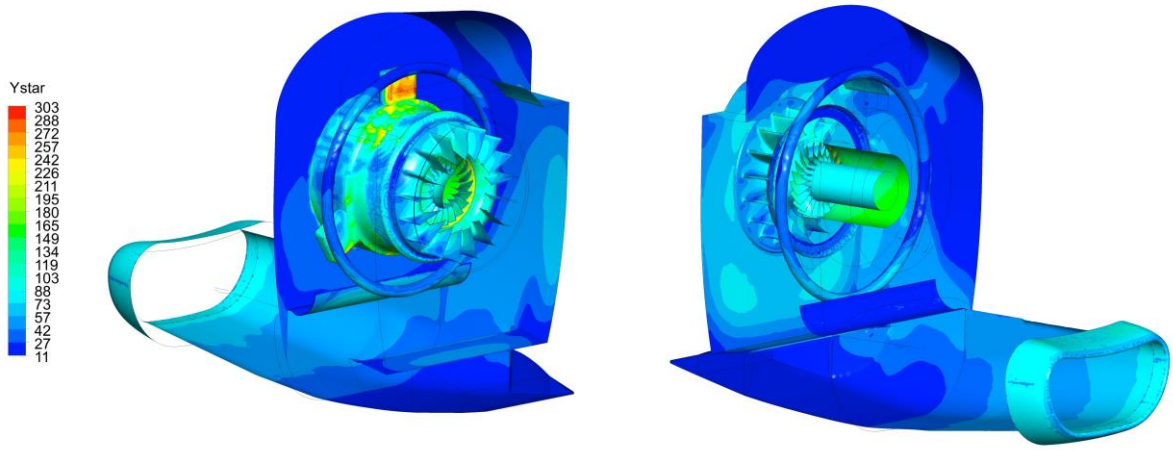

Figure 3.9 – y^* values contoured on domain walls

Solution independency on mesh resolution was not tested with grid containing double the number of elements. Only reason was great computational cost using initial mesh. However, in further study, mesh independency study is highly necessary and solution must be taken with caution.

3.5 Multiple reference model

Fluent uses stationary frame of reference for resolving flow and heat equations in standard tasks by default. However, to achieve steady state solution for problem containing rotating parts, involvement of moving frame of reference is needed. It is necessary to split domain to separate cell zones with boundaries – interfaces. Then, rotational or translational speed can be assigned to cell zone. At the interfaces, transformation of flow variables occurs from stationary reference frame to moving reference frame and vice versa. Fluent software offers two steady state methods how to treat cell zone interfaces. It must be stated, both are only approximate methods.

For turbomachinery purposes, recommendation is to use simpler of them – The Multiple Reference Frame Model (MRF) called also 'frozen rotor approach' method, (AFTG, 2013, sections 2.1 – 2.3).

3.6 Numerical setup

For IPS complex geometry, steady state solution of flow field was desired. Due to expected compressibility effects, density-based solver was chosen. As BFS benchmark study showed, either Realizable $k-\varepsilon$ or SST $k-\omega$ models should be reasonable choice for modelling the turbulence. Both models were tested for IPS study, however RKE model performed better in terms of convergence and robustness. Final solution was therefore achieved with RKE turbulence model despite the fact SST model is often used in turbomachinery problems (Vinay et al, 2013), (Kalia et al, 2016).

Due to poor convergence, first order discretization schemes were applied to achieve solution. When switching to second order schemes, solution diverged heavily. Calculation was controlled and directed with use of under-relaxation factors and mainly Courant number. Table 3.3 and Table 3.4 show final settings of Fluent solver. Scalable wall function was used with RKE model.

Green-Gauss node-based gradient was chosen as most accurate option for unstructured tetrahedron mesh, ("Introductory Fluent Training: Chapter 5: Solver settings"). Both explicit and implicit formulations were tested during computation, where explicit one was finally chosen due to lower computation time. Disadvantage of explicit formulation is need for low Courant number, which was lowered anyway due to nature of problem. Courant number was gradually increased

during calculation, started at 0.1 and raised to 1.5. All under-relaxation parameters were decreased by 0.2 from default values until solution converged.

To find correct setup of a solver and ensure better convergence, simulation with pressure-based solver and heavy under-relaxed parameters was also carried out with no improvement. Boundary conditions combination and numerical setup were tested at simpler geometry of a tube with IPS-like dimensions and configuration.

Table 3.3 – Fluent solver setup

Solver	Density-Based
Turbulence model	Realizable $k-\varepsilon$
Wall Function	Scalable Wall Function
Formulation	Explicit
Flux Type	Roe-FDS
Gradient	Green-Gauss Node Based
Flow	1st Order Upwind
Turbulent Kinetic Energy	1st Order Upwind
Turbulent Dissipation Rate	1st Order Upwind

Table 3.4 – Fluent controls setup

Courant Number	0.1 > 0.3 > 0.6 > 1 > 1.5
Under-Relaxation Factors	Turbulent Kinetic Energy – 0.6 Turbulent Dissipation Rate – 0.6 Turbulent Viscosity – 0.8 Solid – 0.8

Initialization was done from zero values followed by Full Multigrid Initialization (FMG). This method is based on Fluent Full Approximation Storage (FAS) multigrid approach of joining grid cells into larger cells and thus forming required number of coarser, less computational demanding, grids. This process happens multiple times from most coarse grid to finest level. More on FMG initialization in (AFTG, 2013, section 20.9).

3.7 Convergence

It was expected, gradual increasing of parameters such as mass flow rate at the outlet, rotor revolutions and inlet velocity during calculation would allow solution to converge. That method did not bring desired results and finally, FMG initialization from full revolutions and mass flow rate gave best initial guess and final solution. In final stage of calculation, continuity, energy, x- and y- residuals oscillated around value of 1.5e-3 with amplitude approximately 0.2e-3. The z-velocity residual crossed minimum recommended boundary of 1e-3 and settled at value of 7.5e-4. Mass flow rate at region in front of rotor was monitored and when reached stationary value (ca 60 000 iterations), solution was considered as converged. Residuals are captured in Figure C.5 in Appendix C.

Reason for high continuity and energy residuals could be caused by relatively close initial guess, obtained by FMG initialization. Scaling of continuity residuals is done by worst value obtained by solver in first five iterations. In theory, when already converged calculation is started, continuity residuals would be stuck at value of unity. It must be stated, that solution with high values of all residuals needs to be examined with caution.

3.8 Validation

Solution was validated against provided data by GEAC. These data come from region between the rotor and stator stage (i.e. region directly behind the rotor). Data were obtained by GEAC code determining flow parameters in asymmetry. Therefore, to compare the results and data, parameters had to be taken from several positions and averaged.

Axial, tangential and radial velocity profiles along radial coordinate were taken from 8 positions and averaged. Due to approximated flow field caused by 'frozen rotor' approach, velocity profiles directly behind the rotor were locally disturbed and therefore were taken from the end of prolonged compressor canal as shown in Figure 3.12. Static and total pressures were also averaged from 8 positions, but it was possible to take data directly from behind the rotor.

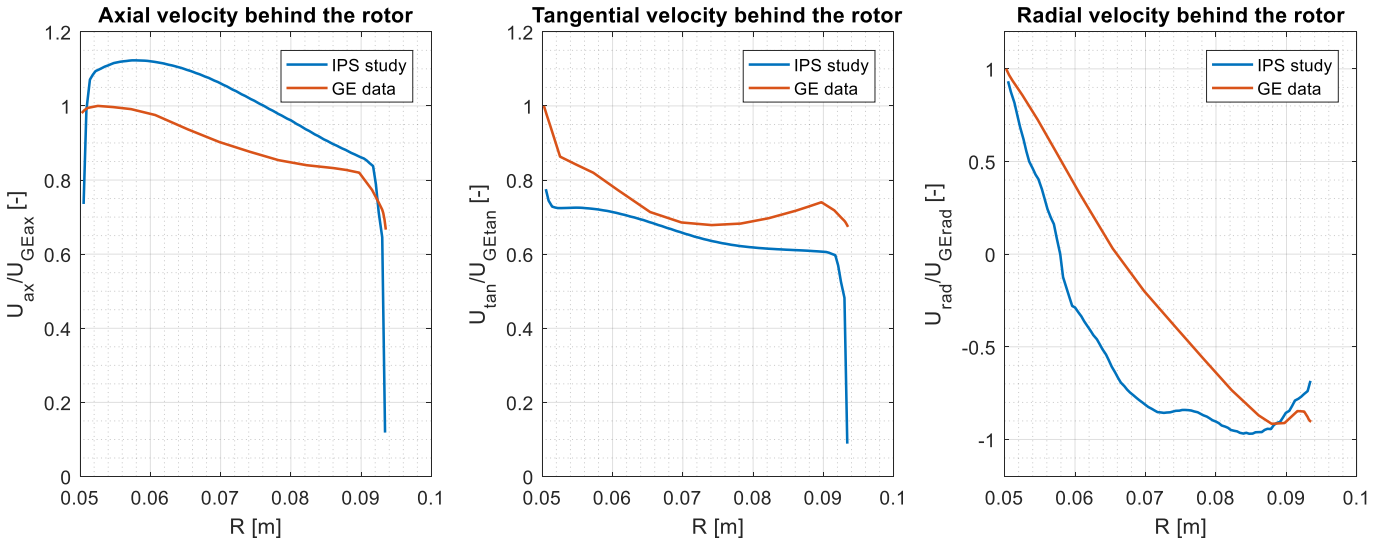

Figure 3.10 – Axial, tangential and radial velocity profiles along the radius at domain outlet, comparison with GEAC data, scaled by maximum value of each variable from GEAC data

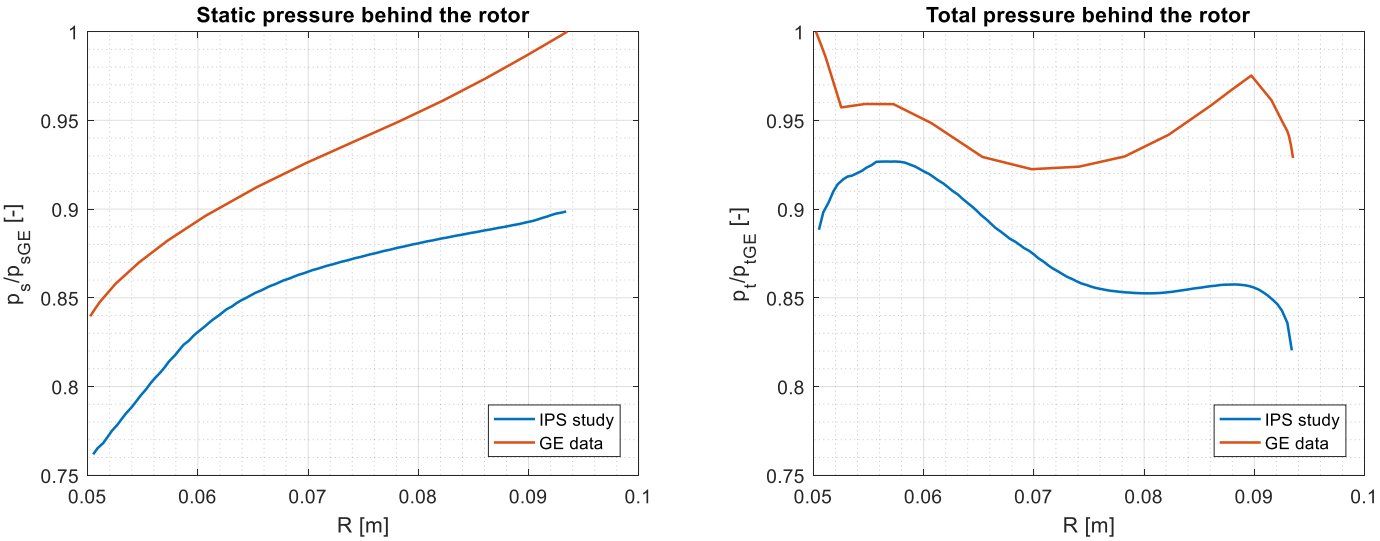

Figure 3.11 – Static and total pressures behind the rotor along the radius of canal, comparison with GEAC data, pressures scaled by maximum value of each variable from GEAC data

In Figure 3.10 can be seen that axial velocity is circa 12 % higher than data. On the other hand, tangential velocity is up to 20 % lower. Prediction of radial velocity is shifted and changes from

positive to negative value nearer the hub. Simulated static pressure is approximately 10 % lower than expected and its distribution is in good agreement with data. Total pressure is also about 10 % lower but is more off at the outer radius of rotor as seen in Figure 3.11.

Despite the use of 'only' 1st order interpolation schemes, the shapes of all velocity and pressure profiles agree with provided data and solution can be considered as sufficiently validated for further analysis. Discussion about differences between simulation and data is provided in next chapter with more detailed results.

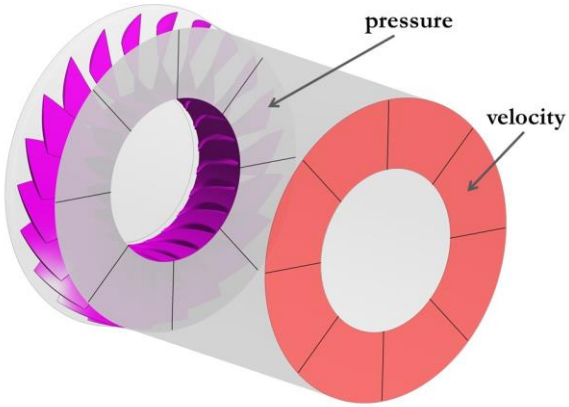

Figure 3.12 – Radial lines for variable readings used for validation, red surface is compressor outlet

3.9 Results & Discussion

Streamlines in Figure 3.13 show air uniformly entering engine intake. No separation is visible in diffuser area. Majority of flow enters compressor at lower part of strut region. Lower number of streamlines in stilling chamber indicates slowed flow. Flow is recirculating in region above inertial separator (marked by red circle). Flow is well attached to separator vane and accelerates as is sucked into compressor, also seen in Figure 3.14, where static pressure drops in proximity of separator vane.

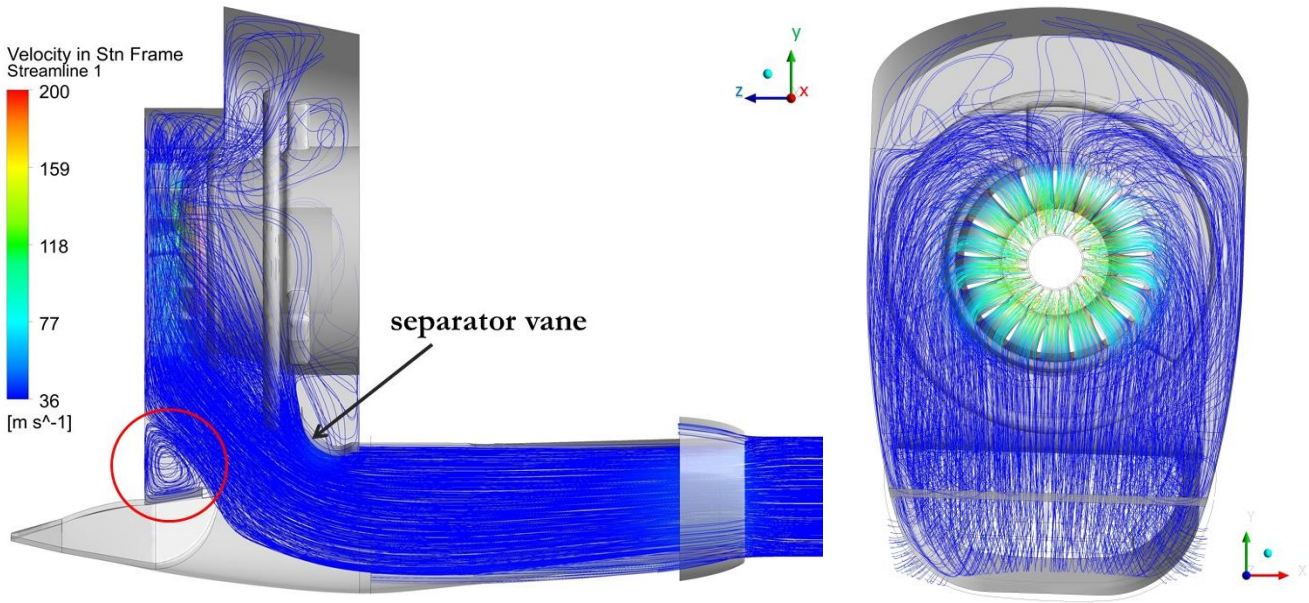

Figure 3.13 – Velocity streamlines visualizing flow inside diffuser and stilling chamber entering compressor

In diffuser as expected, static pressure is approximately atmospheric and increases slightly as the flow slows down. Before flow enters compressor, it accelerates rapidly, especially at outer radius wall, which causes large drop in static pressure, seen in Figure 3.14 and Figure 3.16. Total pressure is highest in free stream area, whereas in regions where flow separates, it drops slightly, clearly seen in stilling chamber region.

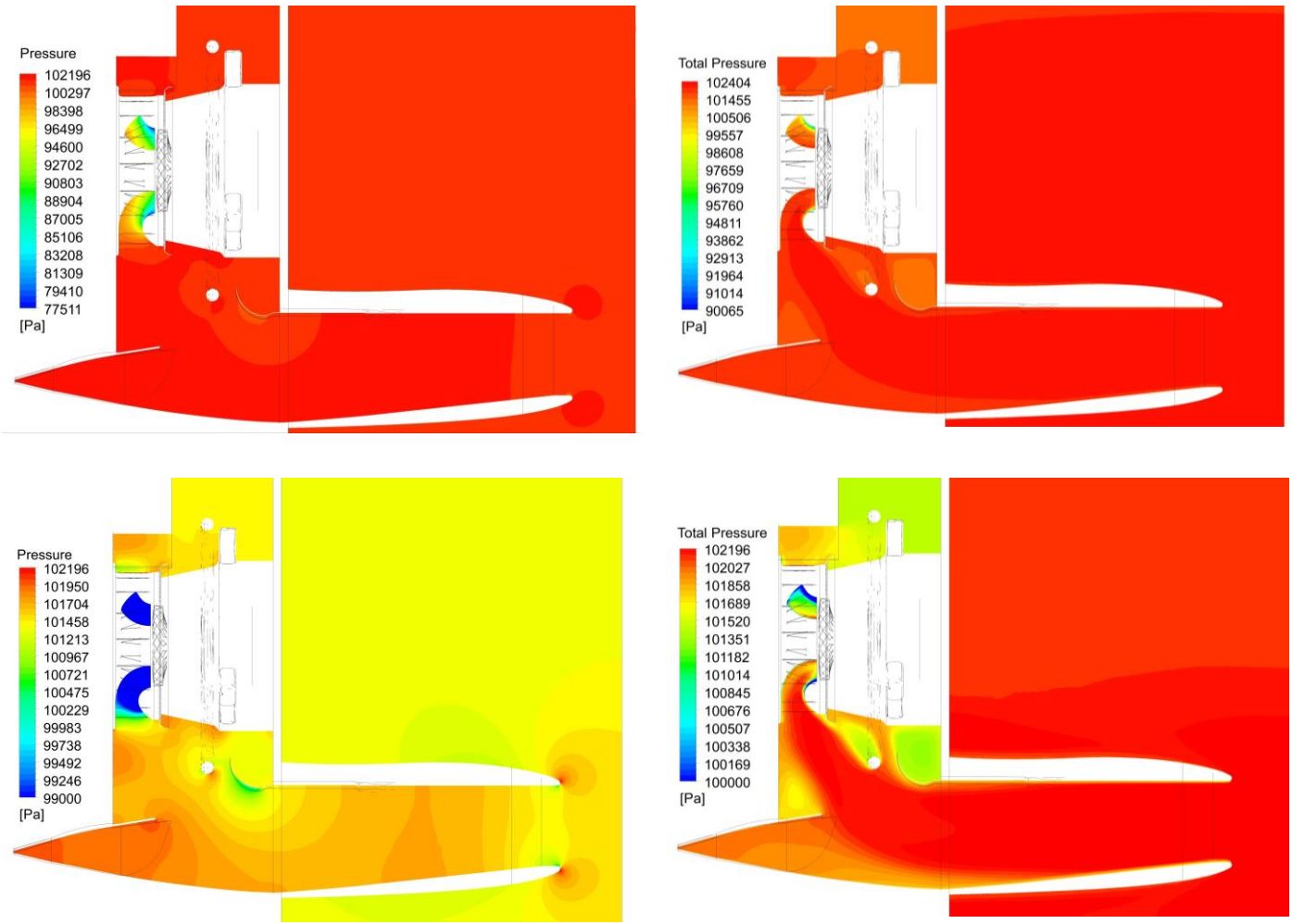

Figure 3.14 – Static pressure and Total pressure contoured at yz plane with x-coordinate = 0, left to right respectively, upper figures with local range of pressures, bottom figures with shifted borders of contours to visualize more subtle changes in diffuser area

Pressure distributions at rotor region are showed in Figure 3.15. Static pressure is decreasing as flow accelerates and reaches rotor. Sudden pressure increase is clearly visible behind rotor as flow is compressed. Lowest pressure can be seen at surfaces directly behind the leading edge of the blades. Static pressure is low at the hub of compressor due to its rotation and increases towards shroud whereas total pressure decreases towards the shroud as seen in Validation section. This is caused by difference in velocity along radial coordinate, where highest absolute velocity is at the rotor hub. As stated before, overprediction of axial component of velocity in the rotor region is possibly caused by solver keeping desired the mass flow rate at the outlet BC.

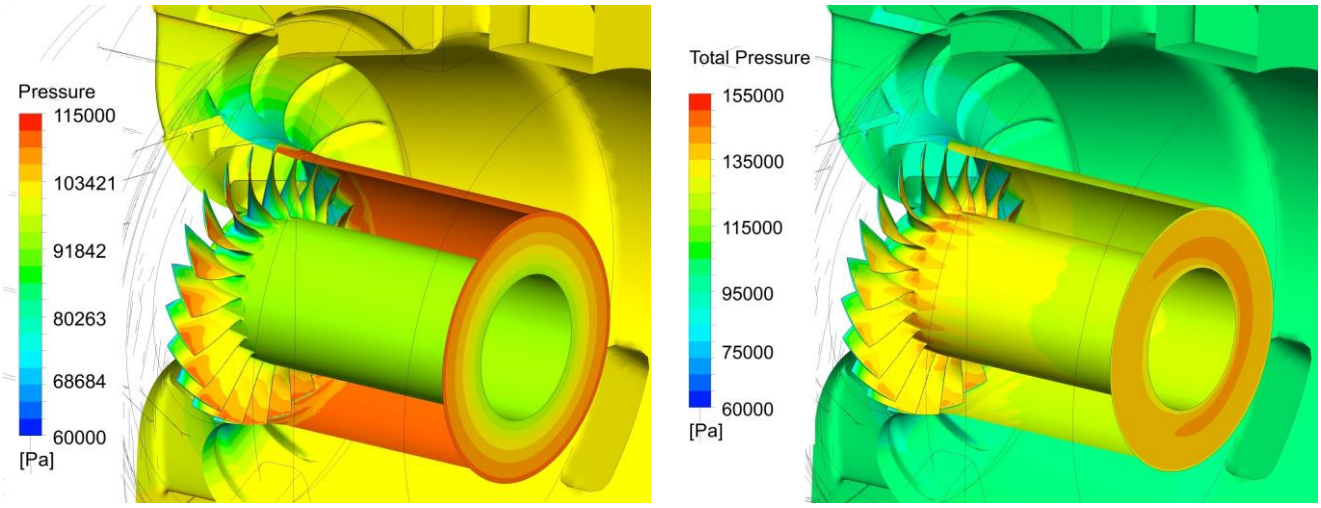

Figure 3.15 – Static pressure and Total pressure at rotor region, left to right respectively

Figure 3.16 depicts absolute velocity field in stationary cell zone in two planes. Velocity field does not vary significantly spanwise. Again, recirculation areas can be spotted in IPS region, above the separator vane and in top part of stilling chamber. Peak of velocity is clearly visible at outer radius of strut section, this is in good agreement with velocity distribution in (Horký, 2011, Figure 8).

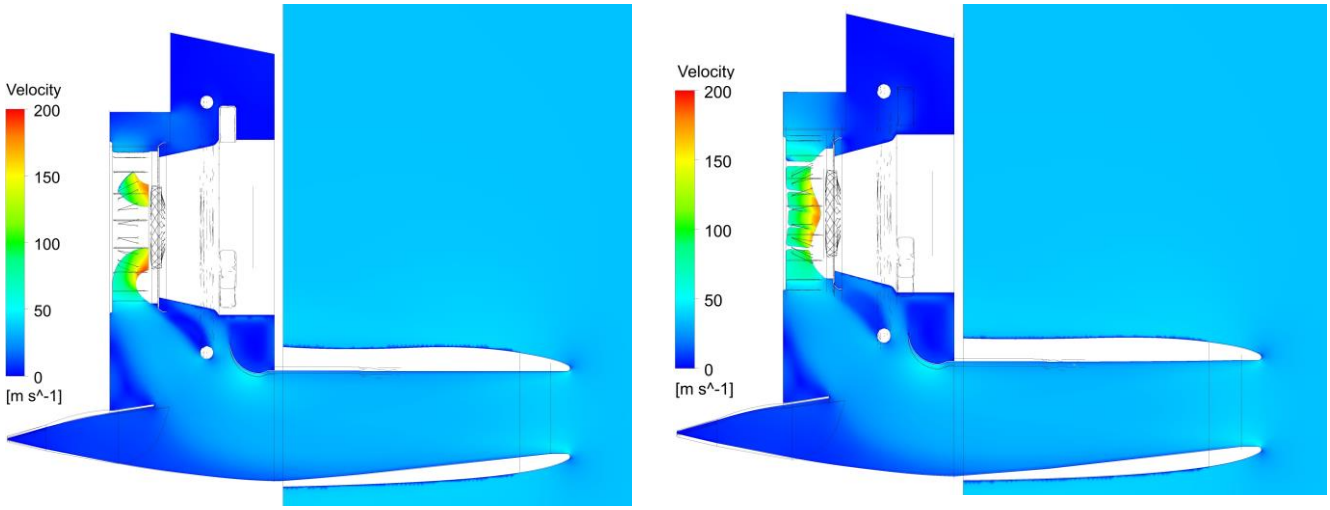

Figure 3.16 – Velocity field contoured at yz plane with x-coordinate = 0 and 0.1 m

Figure 3.17 shows visualization of vortex structures done by Q-criterion (value 0.001). Great recirculation area can be seen in corners of stilling chamber as U-shaped structure. This structure is already mentioned in first paragraph and is cross-sectioned in Figure 3.13 in red circle. Higher values of eddy viscosity ratio also show where turbulence is being modelled by two-equation turbulence model. Another smaller vortices are being produced at the edges of separator vane and behind the mounting ring.

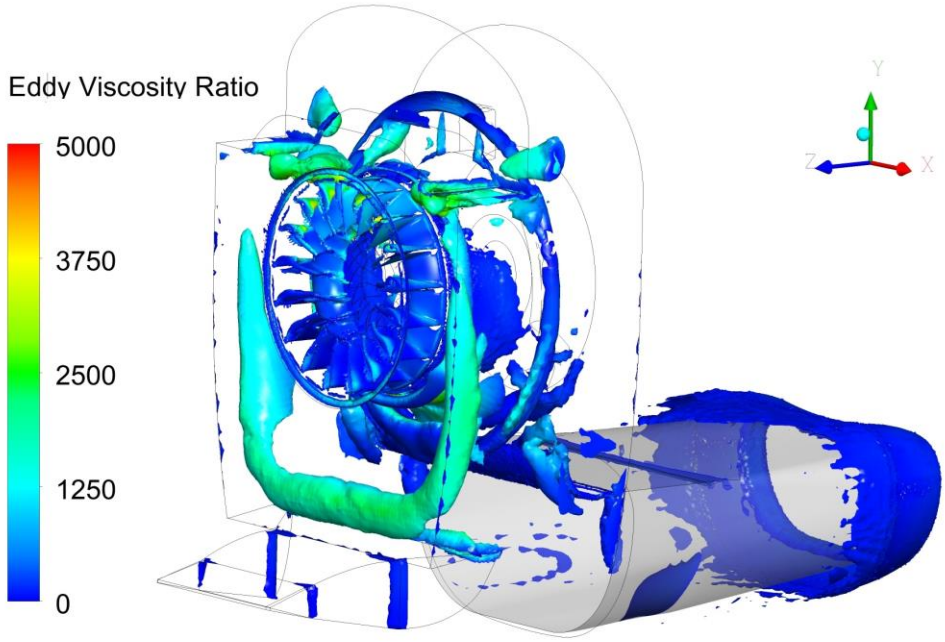

Figure 3.17 – Vortex structures visualized with Q-criterion, contoured with eddy viscosity ratio

4 Particle Tracking Analysis

4.1 Introduction & Assumptions

One of the aims of particle tracking analysis (PTA) in engine intake geometry is to correlate simulated data with real measured damage on compressor rotor and introduce methodology of particle tracking inside turboprop engine with CFD tools, which can be later utilized in IPS design process. Another aim is to investigate possible behavior of particles in present IPS design.

After obtaining flow field parameters in the domain, PTA is possible. To conduct such study, it is convenient to employ several assumptions which simplify further investigation. Due to stochastic behavior of particles in real world and number of possible setups in simulation, statistic approach is necessary for result evaluation.

Random behavior (bounce-off, etc.) of particles given by irregular shape is neglected by assumption of spherical particles. The spherical shape simplifies drag calculation and collisions of particles with domain walls as discussed later in this chapter. The bounce-off is further simplified by assuming no disintegration of particle during impact and no rotation of particle before and after bounce. Also, it is neglected effect of the protective metal grid which is situated in front of strut section and possibly causes further randomness in particle trajectories. Detailed information about particle parameters and coefficient of restitution, employed in this specific study, is provided later. Particles were tracked with influence of gravitational acceleration (in direction of negative y-coordinate) and were one-way coupled with the flow.

4.2 Stokes number

Size and density of the particles are key parameters which determine behaviour of particles in fluid flow. To describe and predict particle movement depending on fluid flow, non-dimensional Stokes number (St) is used. As shown in Figure 4.1, very small particles with St bellow unity are carried by flow and maintain its velocity, i.e. they are responsive. On the other hand, larger particles are unresponsive and keep their momentum as eddy does not influence their path. Particles with St around unity can be partially responsive.

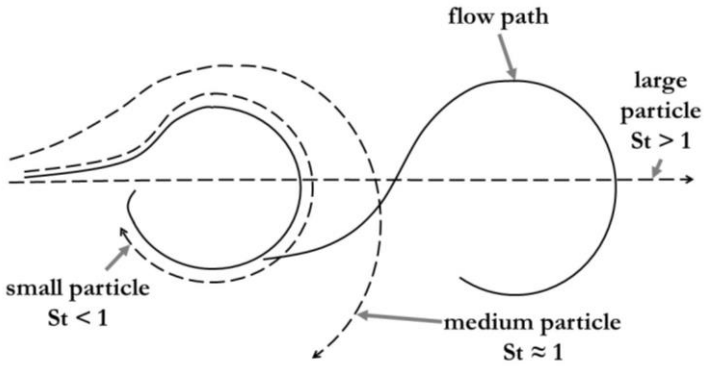

Figure 4.1 – Influence of Stokes number on behaviour of particle in flow field, adopted from (Crowe, Chung, & Troutt, 1988, p. 175)

Stokes number is defined as

$$St = \frac{\tau_p}{\tau_e} \tag{4.1}$$

where τ_p is particle response time. For movement of solid particles with negligible Reynolds number ($Re_p < 0.2$) in gaseous medium, τ_p can be defined as

$$\tau'_p = \frac{\rho_p d_d^2}{18\mu} \tag{4.2}$$

For particles with 0.2 < Re_p< 500 according to Holland and Bragg (1995) or even up to 700 according to Fessler et al. (1999), the particle response time formula is corrected and calculated empirically

$$\tau_p = \frac{\tau'_p}{(1 + 0.15Re_p^{0.687})} \tag{4.3}$$

τ_e is a representative flow timescale presented by Crowe et al. (1988)

$$\tau_e = \frac{l_e}{u_e} \cong \frac{d_{intake}}{U_z} \tag{4.4}$$

where u_e is velocity difference across flow layer and l_e is a representative size of a flow structure, i.e. length scale of energy containing eddies presented by Elghobashi (1994). Definition of representative flow timescale varies depending on case.

For IPS case, flow timescale was calculated as ratio of engine intake dimension (vertical) and axial velocity assigned to inlet BC as shown in eq. (4.4). This estimate applies for particles located directly in front of intake nacelle after injection to domain from inlet surface and describes measure of responsiveness to assumed flow structures. Figure 4.2 shows range of estimated St in dependence on Re_p for smaller of investigated particles. Every curve is bounded by difference of particle and flow velocity from eq. (2.3). It can be seen, smallest investigated particle with diameter of 0.3 mm will be unresponsive after injection with lowest Stokes number around 10. Larger particles are more unresponsive and therefore were not added to figure. Note that unresponsive particles are still being influenced by the flow in larger scale.

Dashed line in Figure 4.2 belongs to St of smallest injected particle recalculated for near compressor region. As seen, measure of unresponsiveness (St) of particles increases with increased flow velocity (Re_p).

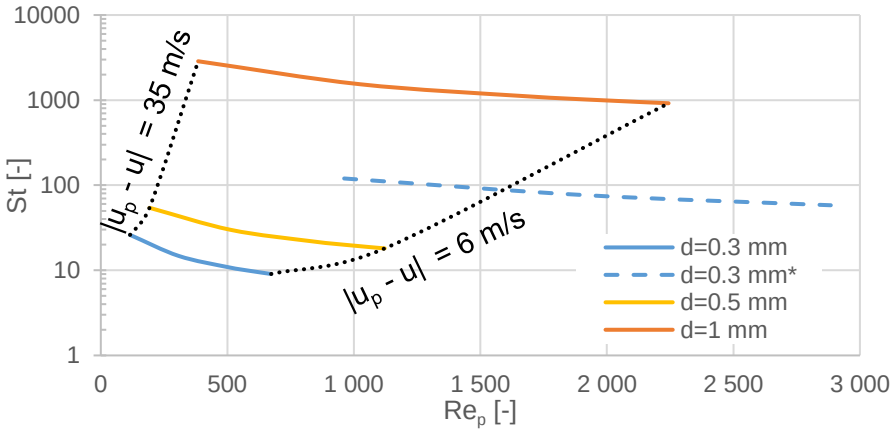

Figure 4.2 – Stokes number as a function of particle Reynolds number for several dimensions of particles located in front of engine intake, bounded by difference in particle-flow velocity, *particle located in front of compressor stage (higher flow velocity)

Particles change their velocity during movement through engine, mainly due to collisions with engine walls. Those particles velocity changes lead to change of Re_p and consequently to change of Stokes number. Thus, responsiveness of particles is changed along the trajectory but as shown in Figure 4.2, investigated particles are not expected to be responsive to smaller flow structures.

4.3 Coefficient of Restitution

While particle is ingested to turboprop engine, it eventually collides with inner walls of engine. Apart from gradual erosion of material or direct damage of engine parts, the collision causes the particle to change its path and lose some of its energy. The effect of a bounce is important aspect of particle study analysis.

The amount of energy or velocity lost during the collision is expressed by coefficient of restitution (COR). For purposes of IPS study, it can be defined by eq. (4.5) as ratio of velocities after and before impact and further to be split to tangential and normal components, eq. (4.6). Perfect elastic collision is expressed by $e = 1$ and cannot be higher when target material is stationary. Impingement angle θ_{in} is defined in Figure 4.3 and has significant effect on COR, (Hamed, Tabakoff, & Wenglarz, 2006), (Abedi, 2009).

$$e = \left|\frac{v_{out}}{v_{in}}\right| \tag{4.5}$$

$$e_n = \left|\frac{v_{n_{out}}}{v_{n_{in}}}\right|;\ e_t = \left|\frac{v_{t_{out}}}{v_{t_{in}}}\right| \tag{4.6}$$

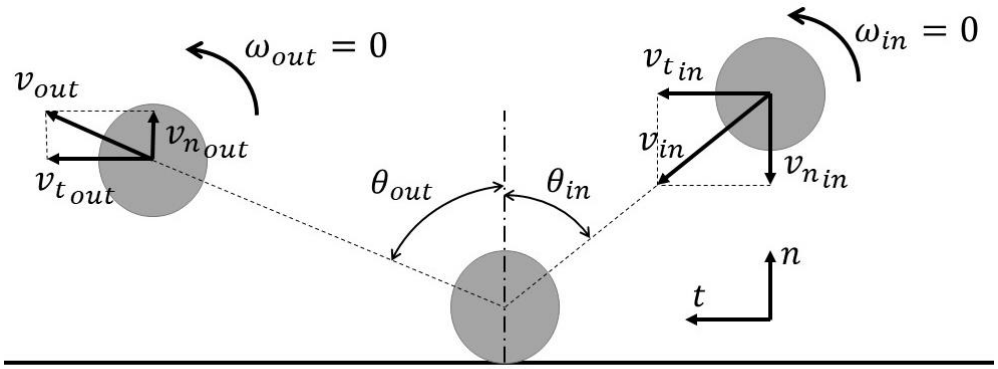

Figure 4.3 – Impact of a spherical particle without rotation, adopted from (Hastie, 2013)

Several constant CORs were investigated during IPS study to find the most accurate setup. To simplify coefficient of restitution definition in numerical model, few assumptions had to be taken. Firstly, the same tangential and normal COR was assigned to all walls at a time. In reality, walls have different hardness, surface roughness and primarily are being hit under different impingement angles. Constant COR also means dependence on impingement angle is neglected.

According to study of Abedi (2009), tangent COR depends strongly on particle size whereas normal COR depends strongly on impact velocity. Therefore, it was decided to investigate this effect and run a case with polynomial formulation of both CORs depending on angle θ_{in}. Polynomials in Table D.1 and Table D.2 (Appendix D) were determined numerically for collisions of sand spheres and aluminium flat plate and are shown in Figure 4.4. From those, polynomials in Table 4.1 were chosen for IPS study. Two formulations for normal COR were tested based on already reviewed cases with constant COR values where average impact velocity of particles was in

between 10 and 50 m·s^{-1}. Formulation for tangential COR was chosen due to correspondence of particle size of 0.5 mm and was kept for both normal polynomials. Also, as seen in Figure 4.4, polynomial for 0.7 mm particle is similar and for larger sizes, information is unknown.

Table 4.1 – Polynomial formulation of normal and tangential coefficients of restitution tested in IPS study, Abedi (2009)

COR	sign	θ_{in}^3	θ_{in}^2	θ_{in}	-
normal (50 m·s^{-1})	e_n50	-1.00E-06	0.0003	-0.0219	1.0951
normal (10 m·s^{-1})	e_n10	-5.00E-07	0.0001	-0.0085	0.9465
tangential (0.5 mm)	e_t500	-2.00E-07	-0.0001	0.0109	0.5867

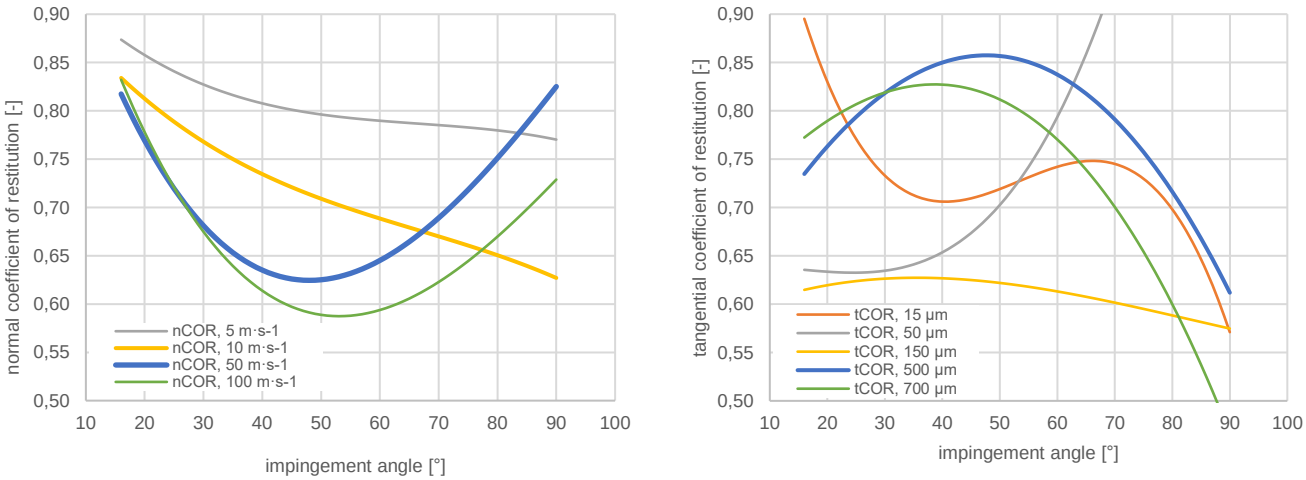

Figure 4.4 – Polynomial formulations of normal and tangential coefficient of restitution, Abedi (2009)

4.4 Investigated particles – Case description

To investigate most accurate setup of injected particles which would agree with real damage, several dimensions of spheres were tested. Largest investigated particle was chosen to be 2.5 mm due to presence of protective metal grid (seen in Figure 3.1) filtering any objects larger than 3 mm. Lower limit of the particle size was chosen to be 0.3 mm. It was assumed smaller particle is not able to cause damage observed in Foreign object damage (FOD) study (Šimota, 2015) provided by GEAC company. Nature of observed damage is showed in Figure 4.5.

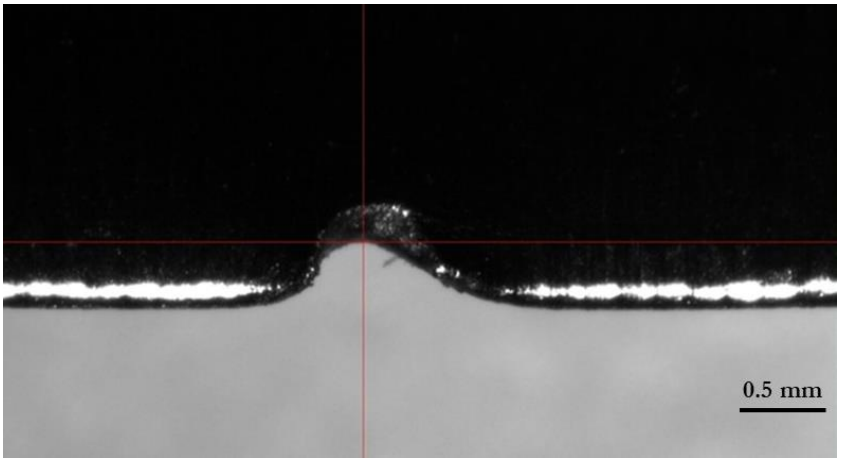

Figure 4.5 – Observed damage at leading edge of rotor blade, adopted from Šimota (2015)

Another parameter significantly influencing particle trajectory is injection velocity, i.e. initial velocity of particles entering the domain. Tested range of injection velocities was decided to be from 1 to 30 $m \cdot s^{-1}$ in normal direction to inlet BC. Due to stationary engine configuration, it was assumed particles entering the engine do not exceed velocity of propeller flow and are in fact lower. Coefficient of restitution was investigated for values of 1 – perfect elastic collision to 0.6. Also, polynomial formulation of COR was tested as described in previous section. Finally, two particle densities were tested, 1800 $kg \cdot m^{-3}$ and 2600 $kg \cdot m^{-3}$ which approximately correspond to gravel or stones present on grass surfaces and asphalt or concrete debris, coming from standard runway, respectively, ("Density of materials", 2016).

Table 4.2 – Overview of tested parameters (420 combinations in total)

Particle size [mm]	Inject velocity [$m \cdot s^{-1}$]	Coef. of Restitution [-]	Density of particles [$kg \cdot m^{-3}$]
0.3	30	1	1800
0.5	20	0.9	2600
1	10	0.8	
1.5	5	0.7	
2	1	0.6	
2.5		polynomial e_n10, e_t500	
		polynomial e_n50, e_t500	

To gather all desired data, particles were injected as follows. One injection contained ca 200 particles of one diameter with one given injection velocity, e.g. diameter of 0.3 mm and injection velocity of 1 $m \cdot s^{-1}$. Second injection consisted of 200 particles of 0.3 mm diameter, injection velocity of 5 $m \cdot s^{-1}$ and so forth. For 6 particle dimensions and 5 injection velocities that means 30 different cases. Later statistic evaluation was done by taking same sized particles (with different injection velocity) together, those shall be called particle clusters.

Density of particles and coefficient of restitution were parametrized. After tracking particle clusters with one COR setup, that was changed, and calculation was repeated for all tested coefficients. Same process was done with density. In total, that gave 14 different configurations for each particle cluster. Overview of all investigated parameters is shown in Table 4.2. Particles were injected from bounded surfaces in front of engine intake nacelle in grid-like configuration of 12 columns and 18 rows, shown in Figure 4.6 .

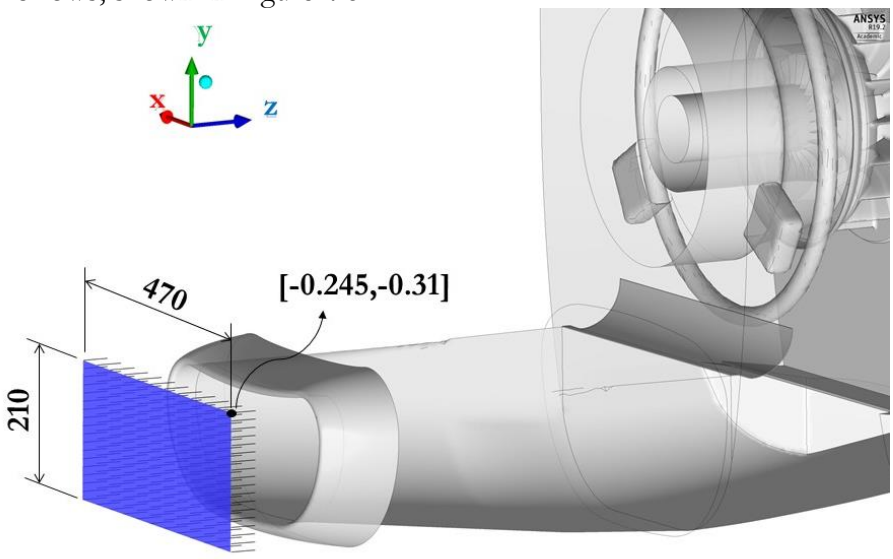

Figure 4.6 – Surface and dimensions from which particles were injected to engine

4.5 Particle observation & Statistics

According to FOD observation by GEAC, majority of debris impacts at leading edge of a rotor blade. Therefore, particles were sampled when in contact with surface of blisk. Data was filtered to evaluate only impacts at leading edge or its proximity and not to include downstream bounces in between the blades. That meant, z-coordinate was limited as shown by grey surface in Figure 4.7. Also, only particles with positive streamwise velocity were included. Figure 4.7 shows path of one particle and its transfer from stationary zone to rotational one. The sudden change of particle trajectory is caused by rotating frame reference.

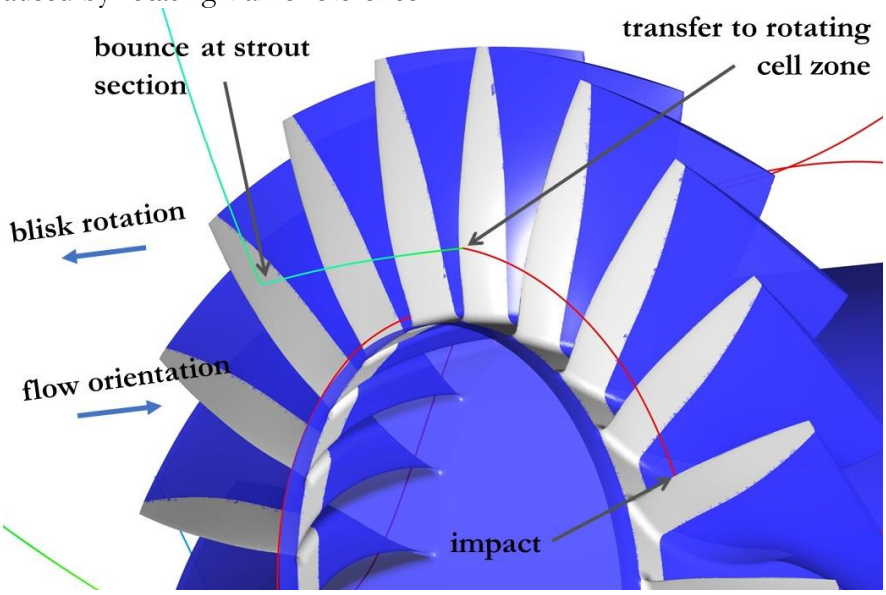

Figure 4.7 – Depiction of observed surface (grey), trajectory of particle and its transfer to rotational cell zone

After particle tracking and sampling, data were gathered into smaller groups defined by particle size. The data were sorted by radial position of impact and distributed into bins (range of 2 mm radially), Figure E.1 (Appendix E) shows example of obtained histogram. Processing of all impacts by that way allowed to compare simulated distributions against the real one. Correlation between those was computed by use of Spearman's rank correlation hypothesis which can be used for non-normal distributed data. Statistical significance was tested by t-test. This method was utilized based on ("Spearman's Rank Correlation Hypothesis Testing", 2012).

4.6 Results & Discussion

4.6.1 Correlation to real damage

Computed correlations of all simulated cases to real FOD at rotor are shown in Figure 4.8 and Figure 4.9 for both investigated densities. Computed values for all cases are stated in Table E.1 and Table E.2 in Appendix E.

In both figures, trend of decreasing correlation with increase of particle size can be observed. This could be caused by greater irregularities of larger (real) particles resulting in 'more stochastic' nature of bounce-off or simply by the fact that larger particles are not so commonly ingested. All setups behave approximately the same for both densities, but lower density cases reached slightly higher level of correlation.

Combination of polynomials marked as e_n10 and e_t500 significantly outperforms second combination with e_n50 and e_t500 for two smallest particles and both densities. That is in good

agreement with the fact, that majority of bounces happen well below impact velocity of 50 m·s^{-1}. As seen in set of pictures Figure 4.11 to Figure 4.16, impact velocity is mostly in interval from 5 to 20 m·s^{-1} and therefore formulation of e_n10 should be more accurate. Sudden decrease of correlation, for 1 mm particles and larger, is caused by origin of e_t500 polynomial, derived for particle size of 0.5 mm. All polynomials were derived for sand particles, which may be another reason of relative inaccuracy.

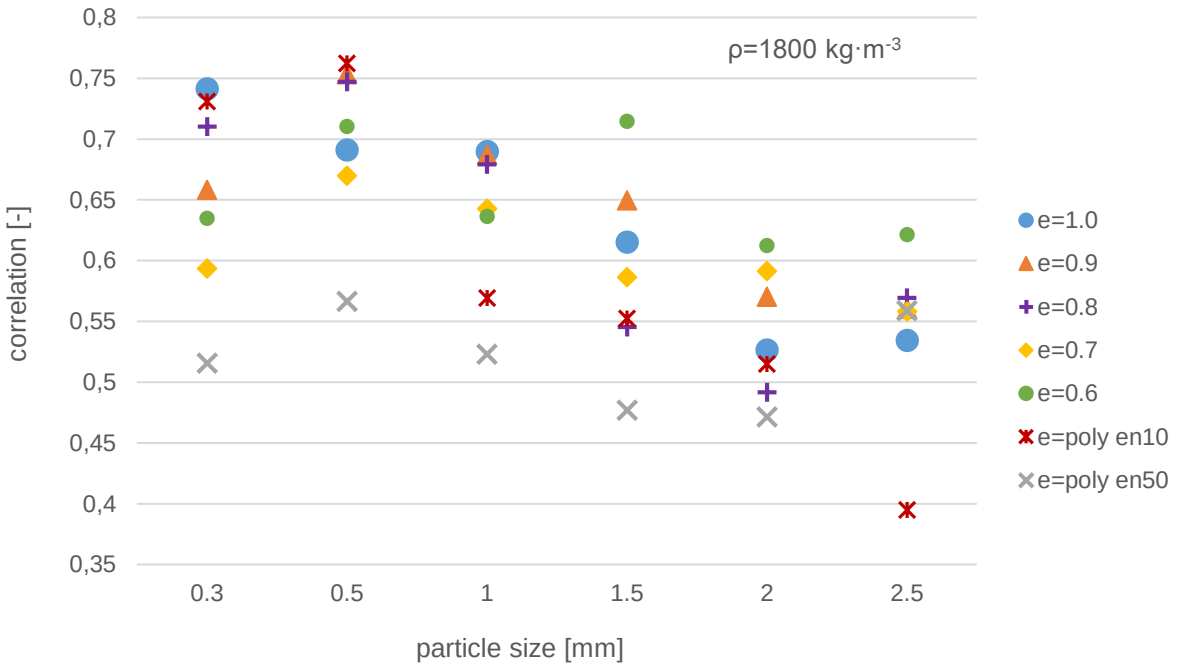

Figure 4.8 – Correlation of simulated cases with real FOD for all particle sizes, coefficients of restitution and density = 1800 kg·m^{-3}

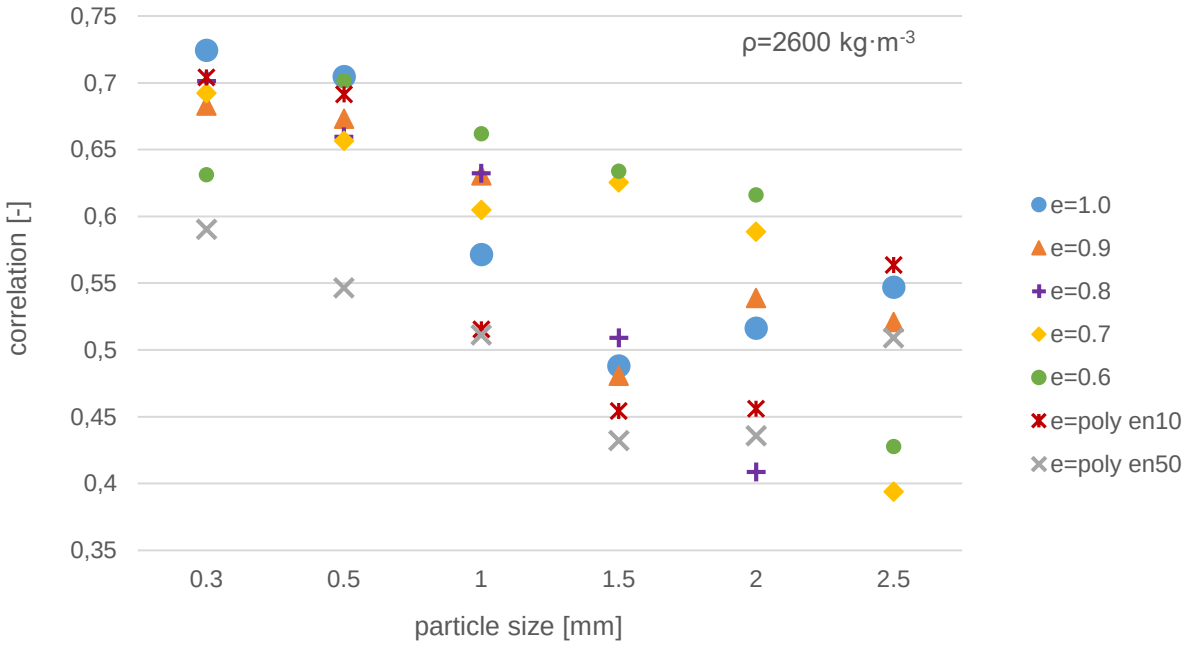

Figure 4.9 - Correlation of simulated cases with real FOD for all particle sizes, coefficients of restitution and density = 2600 kg·m^{-3}

For lower density and for constant COR setups, the e = 0.8 gave overall highest correlation (comparable with polynomial formulation) for small particles, including 1 mm. For larger particles however, correlation decreases dramatically and, in this region, setup with e = 0.6 performs well. For some particle sizes, values of correlations with different COR are similar whereas for other sizes, those are totally different (e.g. e = 1 and e = 0.6 in Figure 4.8). Cause of mentioned phenomenon remains unknown. One possible explanation could be, that constant value matches normal COR in one setup and tangential COR in other and vice versa.

In cases with higher density, apart from polynomial formulation, setups with e from 0.9 to 0.7 are very close to each other for smaller sizes with high level of correlation. Setup with e = 0.6 outperforms others with exception of largest and smallest size. Setup with perfect elastic collision performs exactly opposite. Setup with e = 0.7 seems to be also balanced over all sizes apart from largest.

To investigate effect of injection velocity on final correlations showed above, two particle sizes with given COR and density were divided by the injection velocity and studied separately. Figure 4.10 shows computed correlations. It is clearly visible, particles injected to engine with velocity of 10 m·s^{-1} correlate stronger. Also, it seems the influence of initial velocity is more important with larger particles.

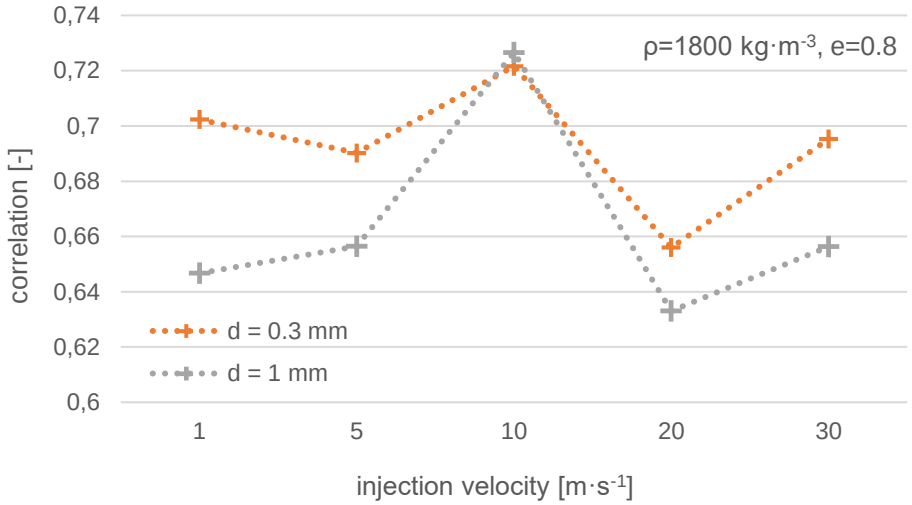

Figure 4.10 - Correlation of specific setup with real FOD for two particle sizes depending on injection velocity

4.6.2 Evaluation of particle trajectories

Series of figures from Figure 4.11 to Figure 4.16 show cross-section view into engine domain and direct comparison of particle trajectories. Two particle dimensions are showed, those were chosen based on high values of correlation presented in previous section. In every figure, same setup for both tested densities, is depicted. Following figure shows same setup with increased injection velocity etc. Not every injection velocity is shown, the rest can be found in Appendix F. Note that trajectories (coloured by particle velocity) are not shown from initial time of injection, but slightly later to keep the figures clear. Added arrows describe characteristic trajectories, dashed ones – trapped particles in IPS, solid ones – ingested particles.

First set of figures depicts behaviour of 0.3 mm particles, second set show 1 mm particles moving through engine intake. Detailed comments are provided in figure descriptions.

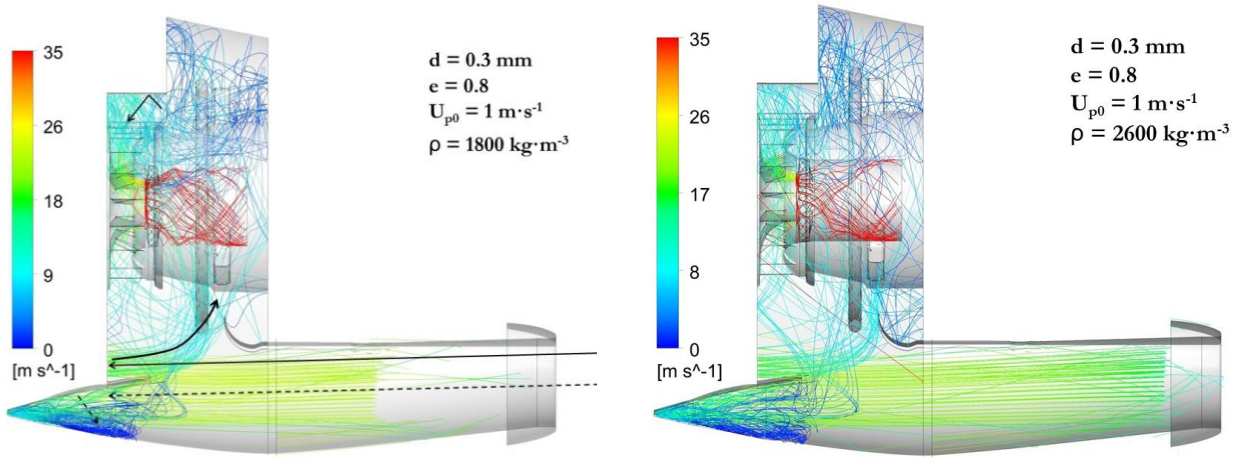

Figure 4.11 – Smallest particles with lowest injection velocity, trajectories are split into two ways. Particles injected into domain at lower position, are trapped in IPS, bounce and finally settle in that region. Some of those bounce and travel upwards. Particles, which missed the IPS, bounce off the stilling chamber wall and are accelerated upwards by flow. Some are ingested immediately, majority bounce in top section of stilling chamber and than are being ingested. Particles with higher density travel in a same manner, increased inertia causes more significant bounce-offs as seen in IPS region.

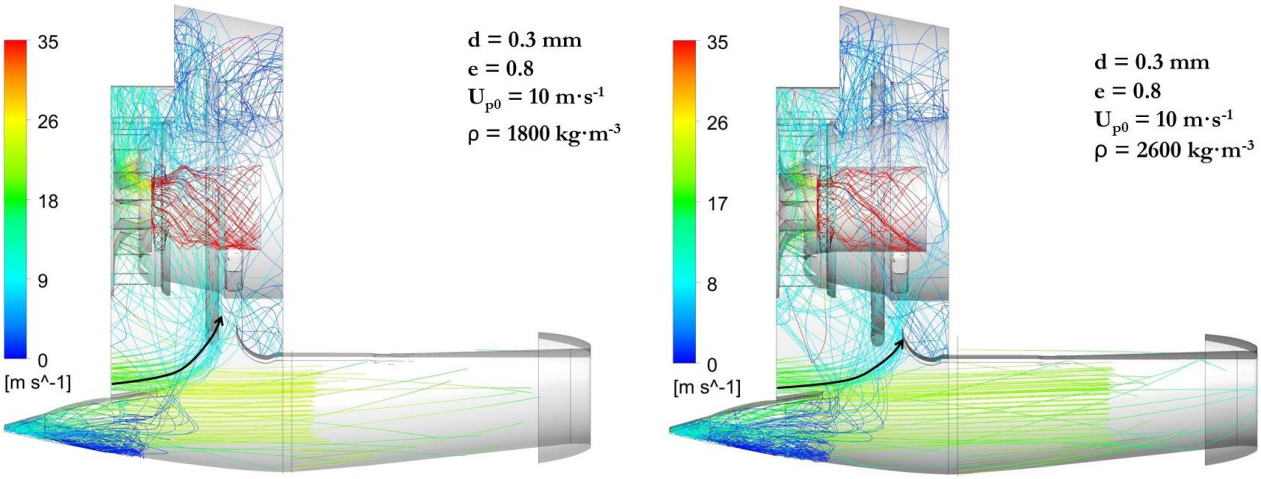

Figure 4.12 – Lighter particles are more accelerated by the flow in diffuser, when they hit the wall above the IPS, they are accelerated and deviated before hitting the separator vane into top section of stilling chamber. Heavier particles hit or nearly miss the top edge of separator vane, there they are influenced by accelerated flow attached to the vane. Particles which hit the IPS bounce in that region and finally are trapped in it.

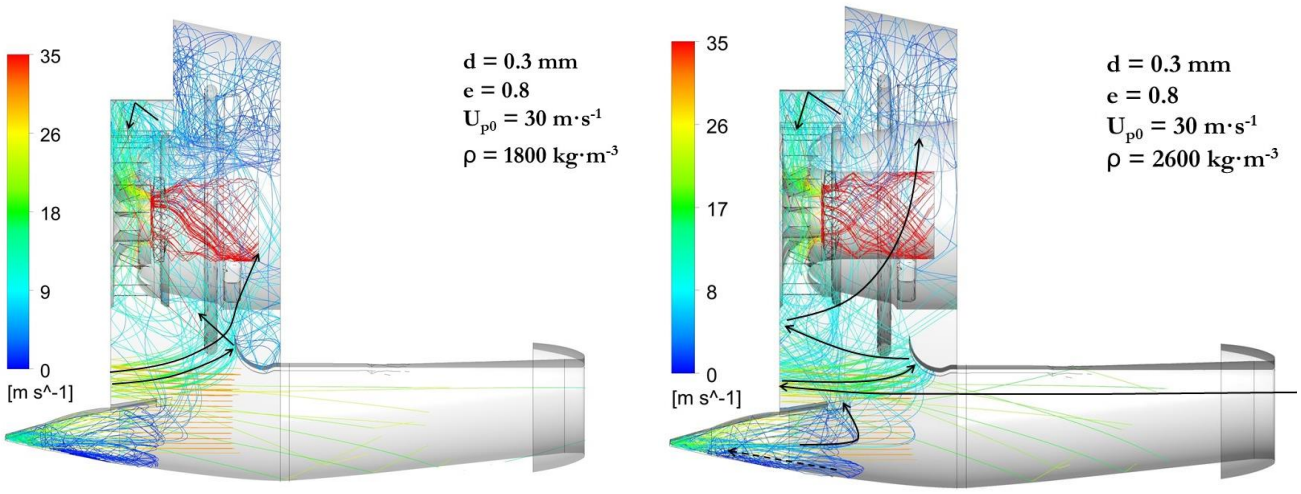

Figure 4.13 – Heavier particles which enter IPS are either being trapped or rebound back into flow and deviate their trajectories into compressor. This process is not that significant with lighter particles due to lower inertia. Compared to lowest injection velocity, particles injected at higher velocity do not lose height inside the diffuser as much and more of those hit wall above the IPS. From the wall they eventually travel (bounce) upwards into stilling chamber or directly into compressor. Lighter particles are being ingested more from upper strut section, note more dense trajectories at that region.

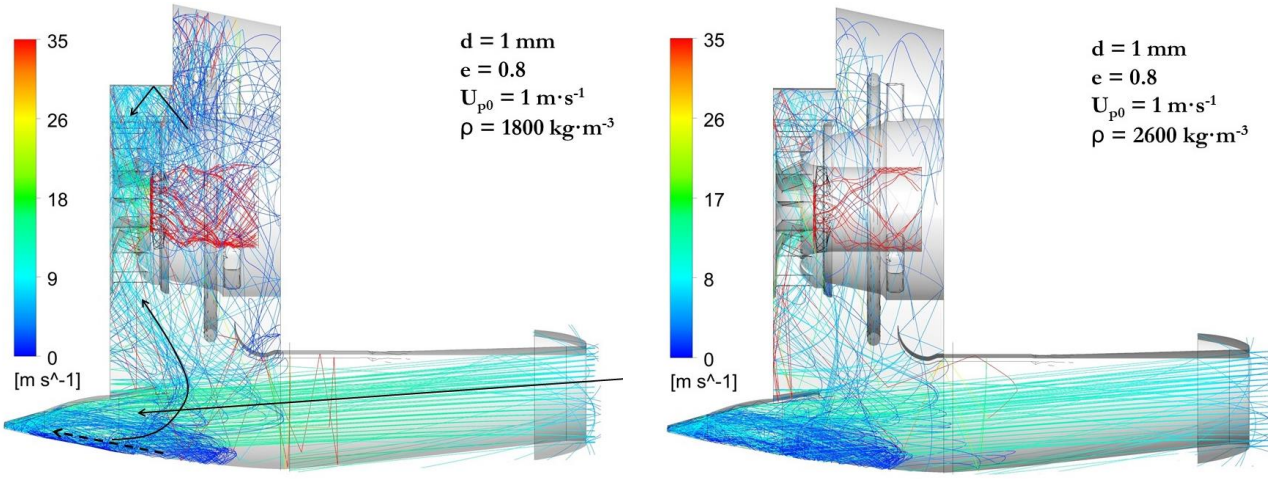

Figure 4.14 – The influence of gravitational acceleration is more significant with larger particles. Particles are being accelerated heavily by the flow due to low injection velocity. Trajectories of more dense particles head down to IPS. From there, some are being bounced back into flow and deviated towards compressor, the rest is trapped in the corner of IPS.

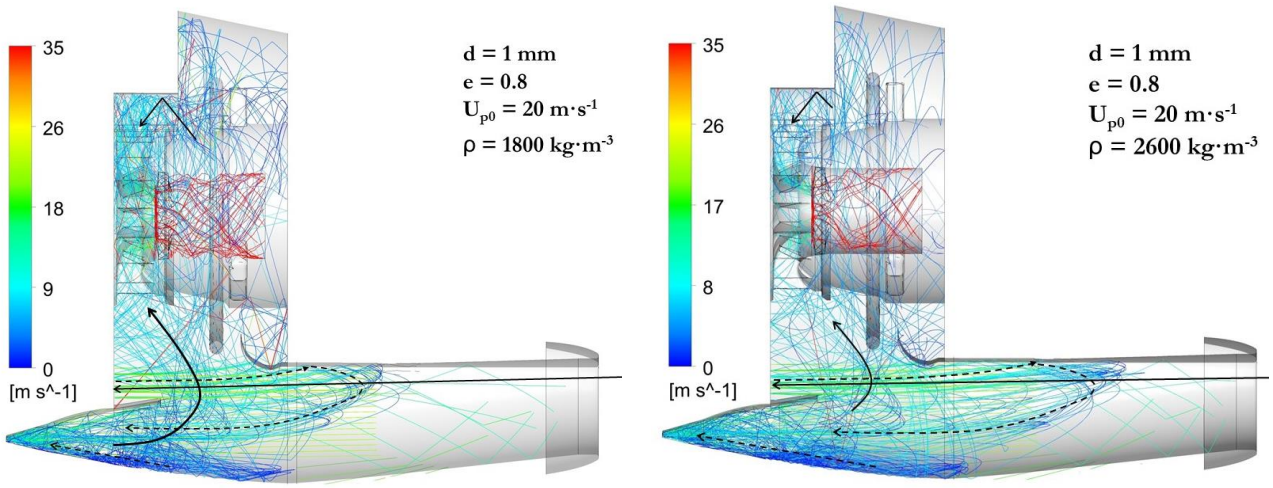

Figure 4.15 – Note higher injection velocity leading to split of trajectories again. Influence of higher inertia is clearly visible where heavier particles bounce from stilling chamber wall and travel far back to diffuser where being decelerated and turned back by flow. As shown by arrows, there the particles are trapped. Some of those particles which hit the IPS immediately are rebound into flow and to top section of stilling chamber.

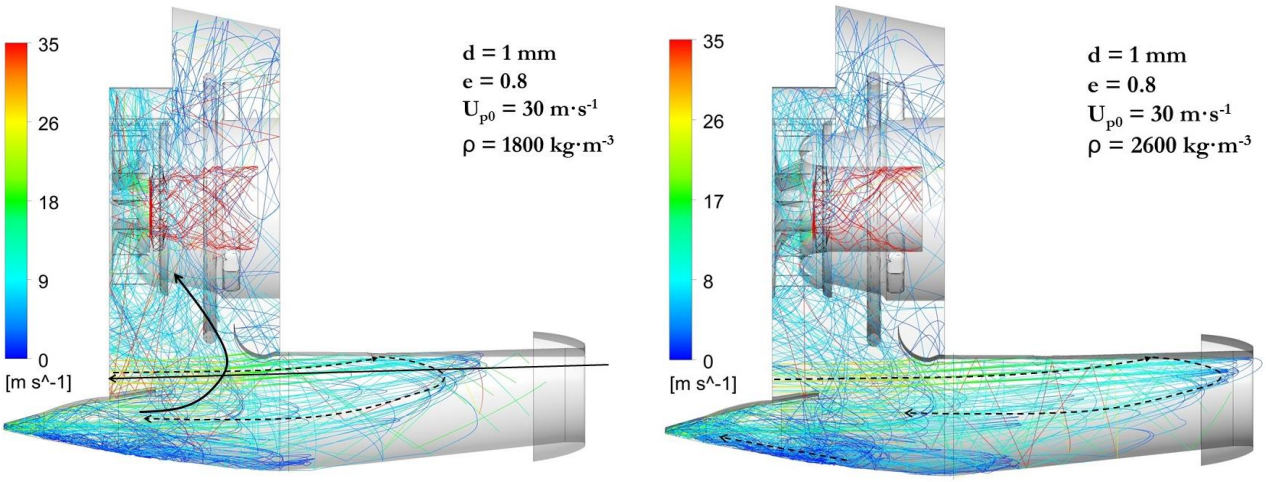

Figure 4.16 – With highest injection velocity, the occurrence of heavy bounce and return of particle to diffuser is even more visible. Some of heavier particles almost leave engine intake. After the turn, particles do not have momentum and mostly are being trapped in IPS. The velocities are high and no clear trend of particle behavior is observed apart from bounce from IPS and deflection by flow into stilling chamber area.

Figure 4.17 shows distribution of particle impacts at rotor blades. Smaller particles impact the rotor close to its hub. The concentration of impacts is dense in top section, meaning particles are being ingested mainly from upper part of stilling chamber. This is in good agreement with observation in Figure 4.12. The distribution for 1 mm particle is more stretched towards blade tips. Ingestion also occurs more from top section of stilling chamber, but the difference is not as significant as with smaller particles.

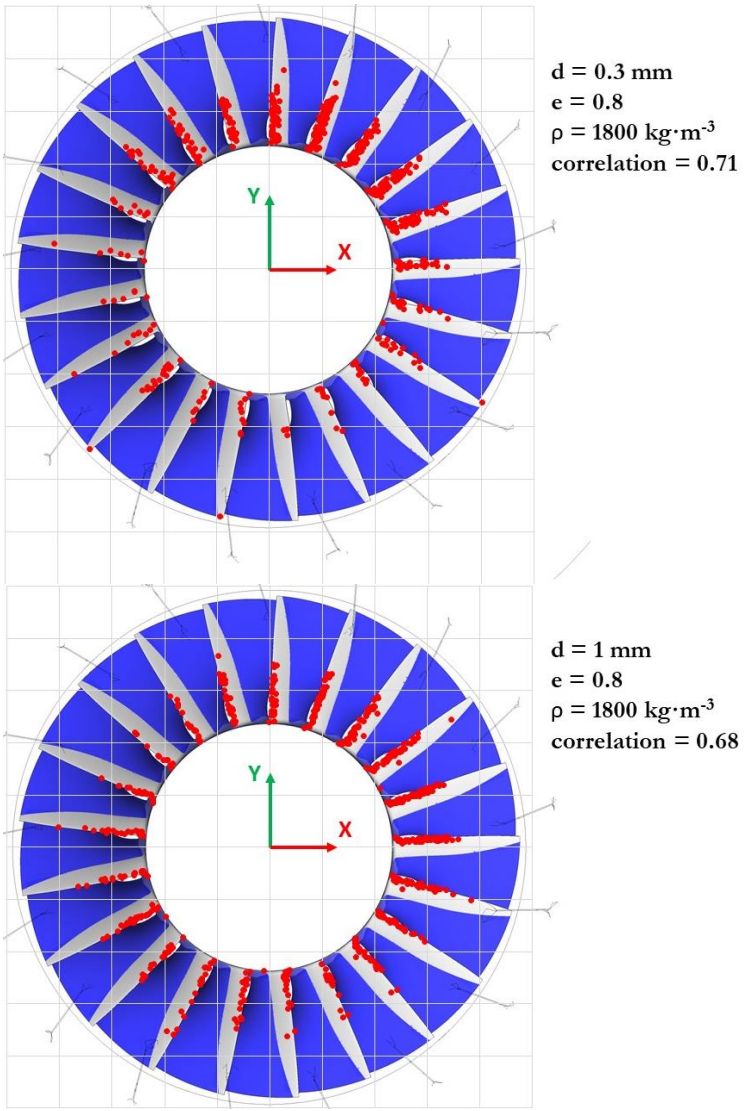

Figure 4.17 – Impact distribution on rotor blades for two particle sizes

Lastly, Figure 4.18 shows present situation with IPS flap closed, particles behave in above described manner. On the right, configuration with IPS flap opened is shown (particles are being trapped by the surface of the flap). Majority of particles hitting the IPS region does not continue in movement around engine intake. The rest is rebound from stilling chamber wall to separator vane and ingested.

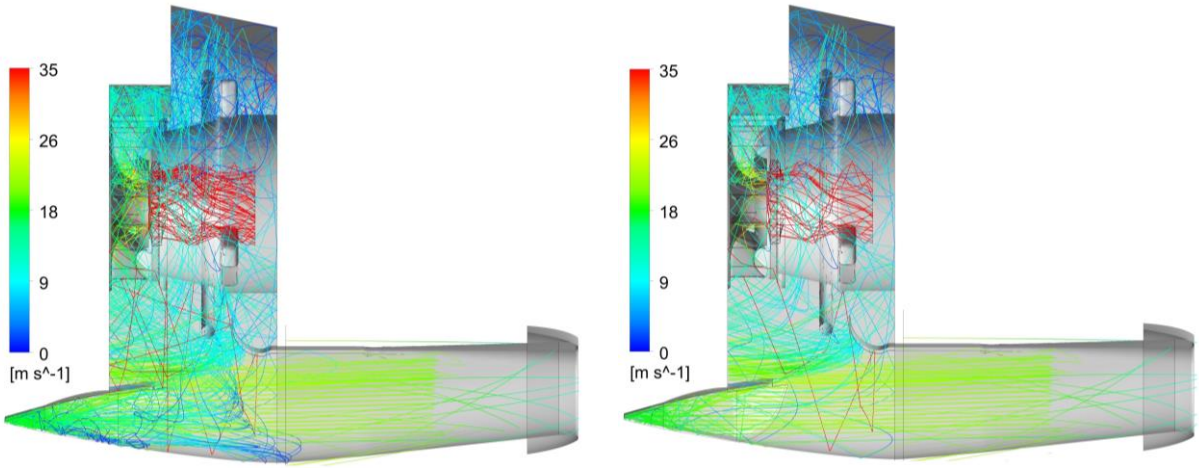

Figure 4.18 – Comparison of configuration with IPS flap closed (left) and open (right)

5 Conclusion

Aim of this master's thesis was to conduct analysis of inertial particle separator situated in a standard turboprop engine. The analysis consists of numerical computation of flow field inside the engine, followed by particle tracking. Purpose of particle tracking was to design viable methodology how to simulate debris ingestion. This procedure can be utilized to evaluate efficiency of inertial particle separator while it is being designed and consequently save costs.

The benchmark study of backward facing step presented at the beginning of the thesis served well for gaining experience with CFD software Fluent. Simulation of flow field and particle movement was validated with experimental data and found to be a reliable tool for further studies. The benchmark study also laid ground for some options for the case setup for future, more complex problems.

During the flow field computations, essential for further particle tracking analysis, several problems occurred, leading to series of adjustments. External part of the geometry had to be enlarged and numerical setup was thoroughly examined. Finally, compressible flow field was obtained throughout the domain with consideration of assumptions such as: no effect of propeller, absence of external geometry of the engine or aircraft. Nevertheless, computed flow field deviated from validation data by 10 to maximum of 20 % and was considered as sufficiently accurate for particle tracking analysis.

Numerical particle tracking analysis presented variation of numerical setups. As a measure of accuracy of each setup, impact locations at 1st rotor of a compressor retrieved by simulation were correlated to observed damage at real parts. Some of the tested setups correlated with real damage on compressor blades with values over 75%. Despite all assumptions, such as simplified inner geometry, propeller-induced flow neglection, spherical shape of particles and others, the strength of correlation is encouraging. It shows the particle analysis can be utilized during inertial particle separator design process.

From the presented analysis can be concluded that particles of interest with the most significant correspondence with real damage probably range from 0.3 to 1 mm. For smaller particles and lower density, the dependence on restitution coefficient is not so strong, unless it is too low. Polynomial formulations of restitution coefficient seem relatively accurate. The drawback is their sensitivity for to specific aspects (particle size, impact velocity, particle density, impact target, etc.). When exact or very close polynomial for the tested particle is unknown, constant value of COR could give more evenly distributed accuracy over wider range of particle size.

The analysis also established that the injection velocity of particles is the main deciding factor of particle velocity throughout engine intake. The flow has a very little influence on particles before their first impact and inertial forces prevail unless particle has low velocity. The particles most probably enter engine intake with velocity around 10 m·s-1.
Visual analysis of strongly correlated setup revealed that inertial particle separator traps portion of particles, whereas some particles only bounce off it and are ingested into compressor. While an aircraft is on the ground, an opened separator flap could lead to further increase of its filtering efficiency.

There is a vast number of variables involved in particle movement through engine area which were not fully investigated, or which were partially neglected and could be included in further studies. Some of those are: angle under which particles are being ingested, rotation of particles before and after impact, effect of particle density or deeper analysis of FOD which could estimate particle size based on indentation left by particle.

Bibliography

Abedi, M. (2009). Effect of Restitution Coefficient on Inertial Particle Separator's Efficiency (Master's thesis). Boston, Massachusetts.

Airplane Flight manual for the L 410 UVP - E20. (1998). Kunovice, Czech Republic: LET. Retrieved May 7, 2019, from http://x-plane.hu/L-410/download/L410%20Flight%20Manual.pdf

ANSYS Fluent Theory Guide [Online]. (2013) (15 ed.). Canonsburg, USA: ANSYS.

ANSYS Fluent User's Guide [Online]. (2013) (15 ed.). Canonsburg, USA: ANSYS.

Chudý, P., Fil'akovský, K., & Friedl, J. (2004). Aerodynamic Analysis of Turboprop Engine Air Intake. *Acta Polytechnica*, *44*(3), 66-70.

Crowe, C. T., Chung, J. N., & Troutt, T. R. (1988). Particle mixing in free shear flows. Progress In Energy And Combustion Science, 14(3), 171-194. https://doi.org/10.1016/0360-1285(88)90008-1

Density of materials [Online]. (2016). Retrieved May 18, 2019, from https://www.simetric.co.uk/si_materials.htm

Elghobashi, S. (1994). On predicting particle-laden turbulent flows. *Applied Scientific Research*, *52*(4), 309-329. https://doi.org/10.1007/BF00936835

Fessler, J. R., & Eaton, J. K. (1999). Turbulence modification by particles in a backward-facing step. *J. Fluid Mech.*, (394), 97-117.

Greifzu, F., Kratzsch, C., Forgber, T., Lindner, F., & Schwarze, R. (2016). Assessment of particle-tracking models for dispersed particle-laden flows implemented in OpenFOAM and ANSYS FLUENT. Engineering Applications Of Computational Fluid Mechanics, 10(1), 30-43. https://doi.org/10.1080/19942060.2015.1104266

Hamed, A., Tabakoff, W. C., & Wenglarz, R. V. (2006). Erosion and Deposition in Turbomachinery. Journal Of Propulsion And Power, 22(2), 350-360. https://doi.org/10.2514/1.18462

Hastie, D. B. (2013). Experimental measurement of the coefficient of restitution of irregular shaped particles impacting on horizontal surfaces. Chemical Engineering Science, 101, 828-836. https://doi.org/10.1016/j.ces.2013.07.010

Holland, F.A. Bragg, R.. (1995). Fluid Flow for Chemical Engineers (2nd Edition) - 9.1 Relative Motion between a Fluid and a Single Particle. Elsevier. Retrieved from https://app.knovel.com/hotlink/pdf/id:kt003JI0Q3/fluid-flow-chemical-engineers/relative-motion-between

Horký, V. (2011). Výzkum a optimalizace rozvíření v radiálně axi- álním vstupním ústrojí s ohledem na dosažení návrhových parametrů a vzájemné spolupráce s prvními stupni axiálního kompresoru malého turbínového motoru [Online]. In Transfer: Výzkum a vývoj pro letecký průmysl (15 ed., pp. 5 - 12). Praha: VZLÚ. Retrieved from https://www.vzlu.cz/cs/15-2011-s592.pdf.

Introductory Fluent Training: Chapter 5: Solver settings [Online]. In . ANSYS. Retrieved from http://slideplayer.com/slide/7295832/release/woothee

Kalia, S., Vinay, C. A., & Hegde, S. M. (2016). CFD analysis of turboprop engine oil cooler duct for best rate of climb condition [Online]. Iop Conference Series: Materials Science And Engineering, 149. https://doi.org/10.1088/1757-899X/149/1/012196

K-epsilon models [Online]. (2011). Retrieved January 31, 2019, from https://www.cfd-online.com/Wiki/K-epsilon_models

Morsi, S., & Alexander, A. (1972). An investigation of particle trajectories in two two-phase flow systems. Journal of Fluid, 55(2), 193–208.

Motory H-Series [Online]. Retrieved May 16, 2019, from https://www.geturboprops.com/cz/motory

Spearman's Rank Correlation Hypothesis Testing [Online]. (2012). Retrieved May 19, 2019, from http://www.real-statistics.com/correlation/spearmans-rank-correlation/spearmans-rank-correlation-detailed/

SST k-omega model [Online]. (2011). Retrieved January 31, 2019, from https://www.cfd-online.com/Wiki/SST_k-omega_model

Sun, D. … et al (2016). Simulation of particle flow in inertial particle separators with Eulerian VR-QMOM method. *AIAA Journal, 54(12)*, 3803-3812.

Šimota, J. (2015). Měření poškození blisku 1. stupně motoru H80 na náběžných hranách lopatek, Výrobní číslo: 140: Zvyšování životnosti a možnosti oprav lopatkových dílů kompresoru z Ti6Al4V v turbovrtulových motorech (Research report). Praha.
v textu: (Šimota, 2015)

Vinay, C. A., Kumar, G. N., Chakravarthy, B., Iyengar, I., & Iyengar, H. N. V. (2013). CFD Analysis of engine air intake for pusher type light transport aircraft [Online]. Retrieved from https://nal-ir.nal.res.in/12470/

Wasserman, S. Choosing the Right Turbulence Model for Your CFD Simulation [Online]. Retrieved from https://www.engineering.com/DesignSoftware/DesignSoftwareArticles/ArticleID/13743/Choosing-the-Right-Turbulence-Model-for-Your-CFD-Simulation.aspx

Parameters and Variables

Parameters and Variables	Description
c_D	Drag coefficient [-]
d_p	Particle diameter [m]
e	Coefficient of restitution [-]
e_{n10}	Polynomial formulation of normal coefficient of restitution for impact velocity 10 $m \cdot s^{-1}$ [-]
e_{n50}	Polynomial formulation of normal coefficient of restitution for impact velocity 50 $m \cdot s^{-1}$ [-]
e_{t500}	Polynomial formulation of tangential coefficient of restitution for particle size 0.5 mm [-]
H	Step height [m]
h	Channel width [m]
k	Kinetic turbulence energy [$m^2 \cdot s^{-2}$]
Re_p	particle Reynolds number [-]
St	Stokes number [-]
U_0	Centerline velocity [$m \cdot s^{-1}$]
y^*	Dimensionless distance from wall [-]
y^+	Dimensionless distance from wall [-]
α_p	Volume fraction of particles [-]
ε	Dissipation rate of kinetic energy [$m^2 \cdot s^{-3}$]
θ_{in}	Impingement angle [°]
μ	Molecular viscosity [$N \cdot s \cdot m^{-2}$]
ρ_p	Particle density [$kg \cdot m^{-3}$]
τ_k	Kolmogorov time scale [s]
τ_e	Large eddy turnover time [s]
τ_p	Particle response time [s]
ω	Specific turbulence dissipation [s^{-1}]

Abbreviations

Abbreviations	Description
AFTG	Ansys Fluent Theory Guide
AFUG	Ansys Fluent User's Guide
BC	Boundary condition
BFS	Backward-facing step
BL	Boundary layer
CFD	Computational Fluid Dynamics
COR	coefficient of restitution
FAS	Full Approximation Storage
FMG	Full Multigrid Initialization
GEAC	General Electric Aviation Czech
IPS	Inertial particle separator
MFR	multiple frame reference
RANS	Reynolds Averaged Navier-Stokes
RKE	Realizable k-ε model
SKE	Standard k-ε model
SST	Shear Stress Transport

Appendix A

Grids used in benchmark study and the rest of velocity profiles used for mesh independency study are shown in following figures.

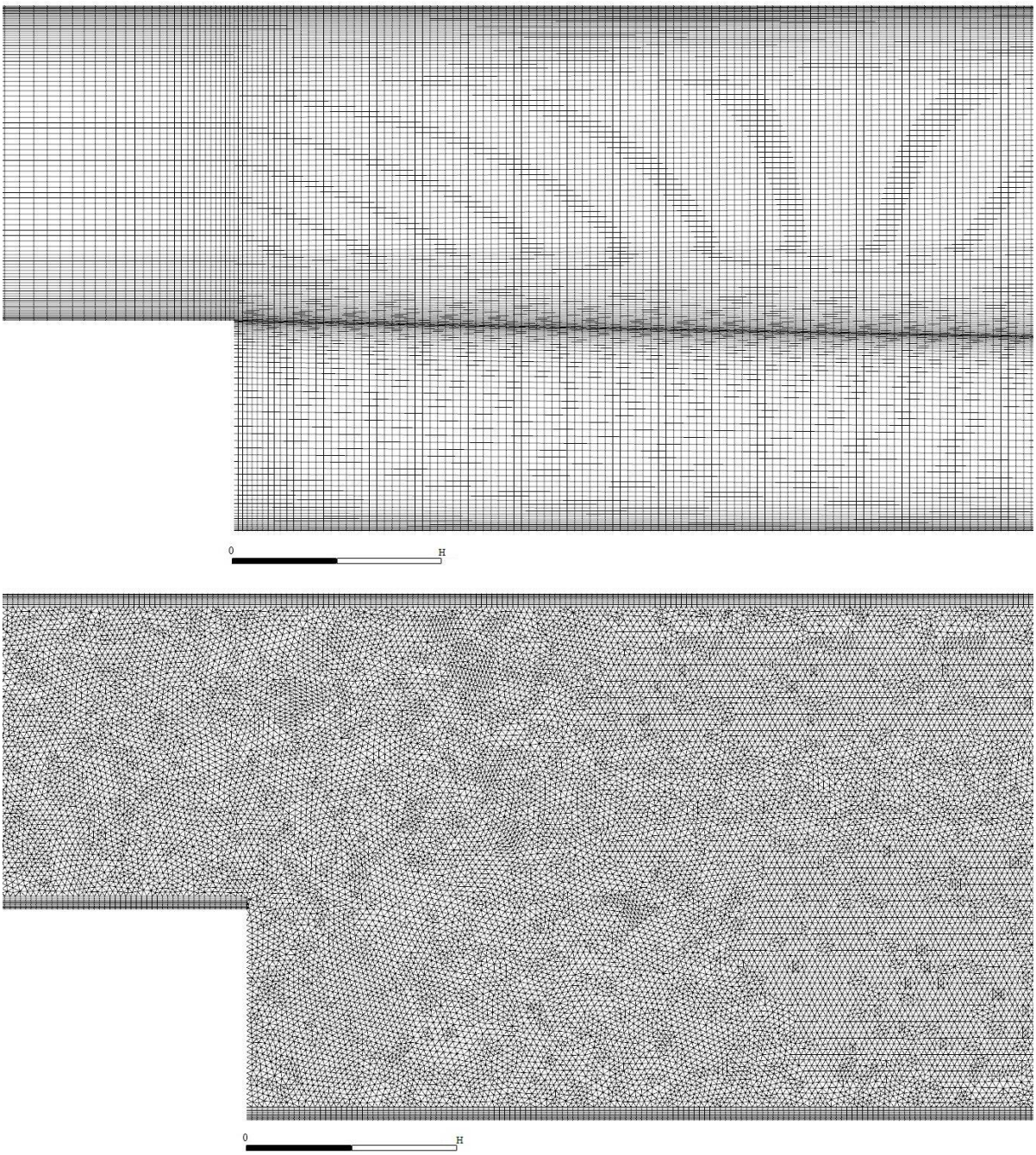

Figure A.1 – Structured and unstructured mesh visualization, step region

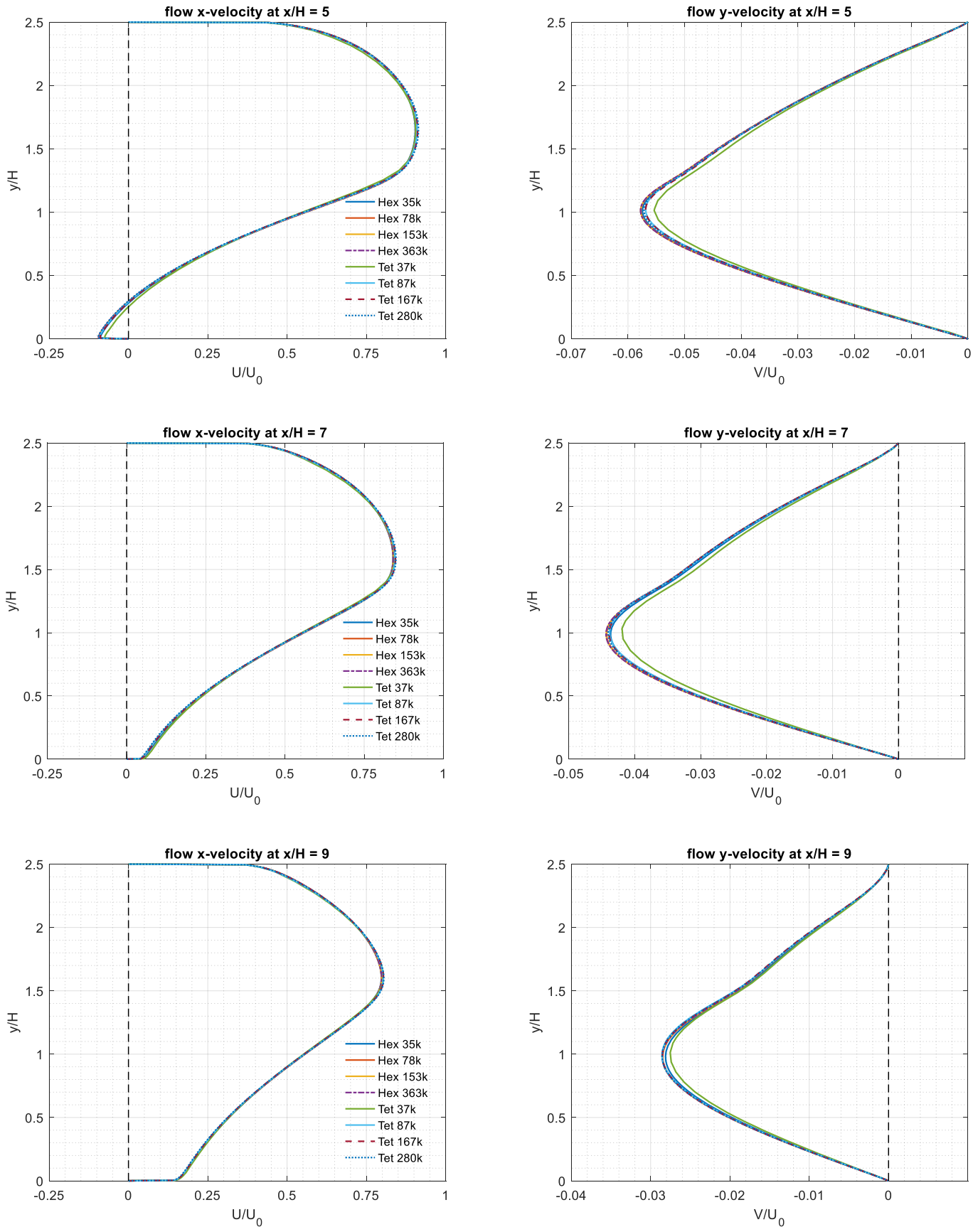

Figure A.2a – Mesh independency, x- and y-direction velocities at x/H=5,7,9

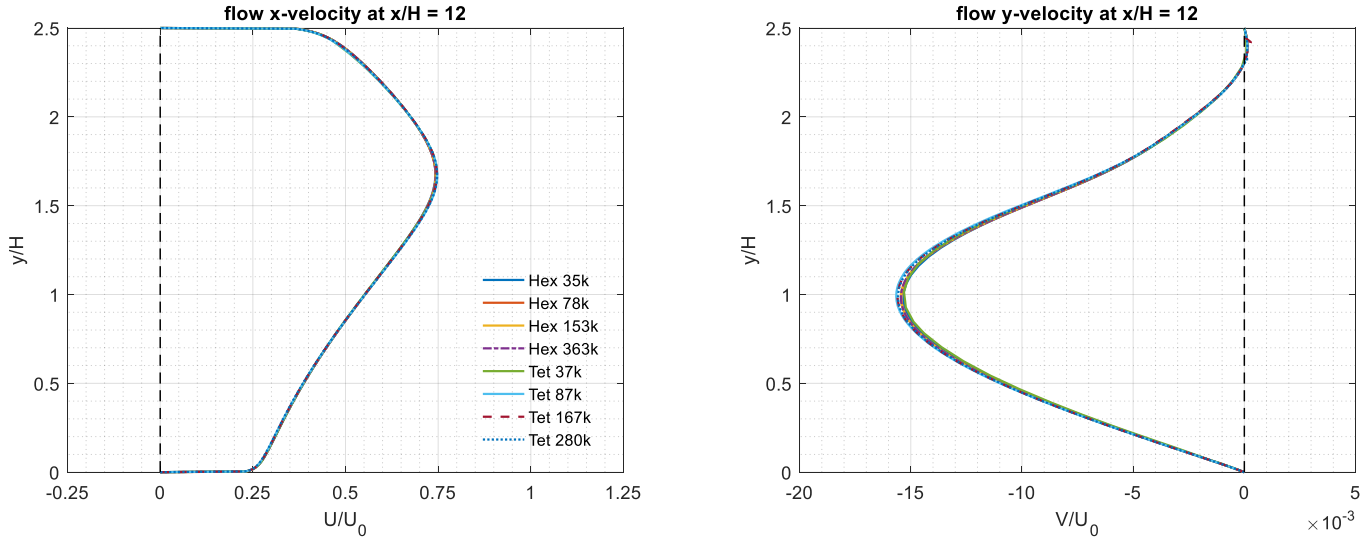

Figure A.2b – Mesh independency, x- and y-direction velocities at x/H=12

Appendix B

The rest of velocity and particle velocity profiles from benchmark study are shown in following figures.

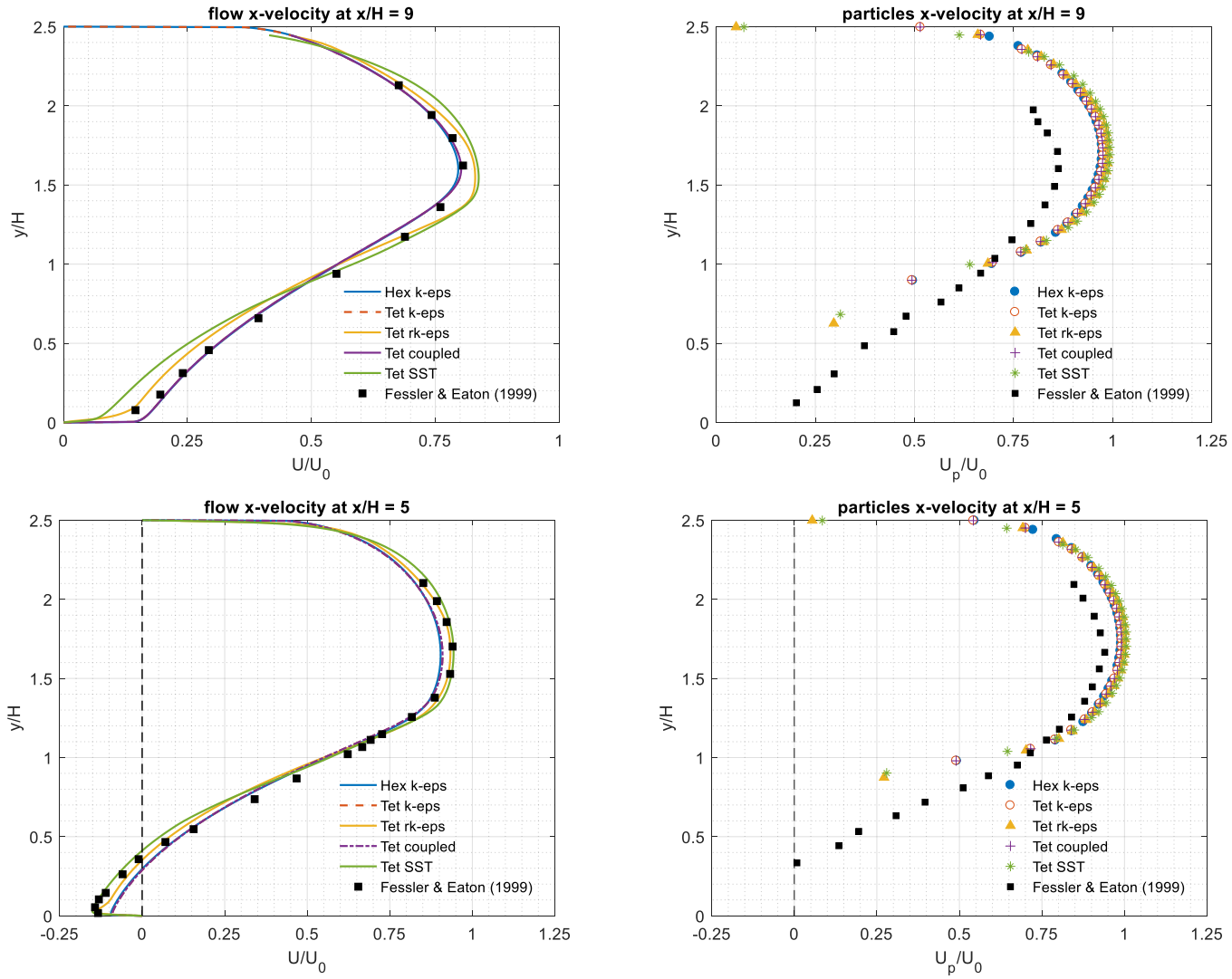

Figure B.1 – Flow and discrete phase velocity profiles at x/H=5, 9; velocities are normalized by centreline velocity U_0

Appendix C

Following figures depict computational grid with 45 million elements used in IPS study.

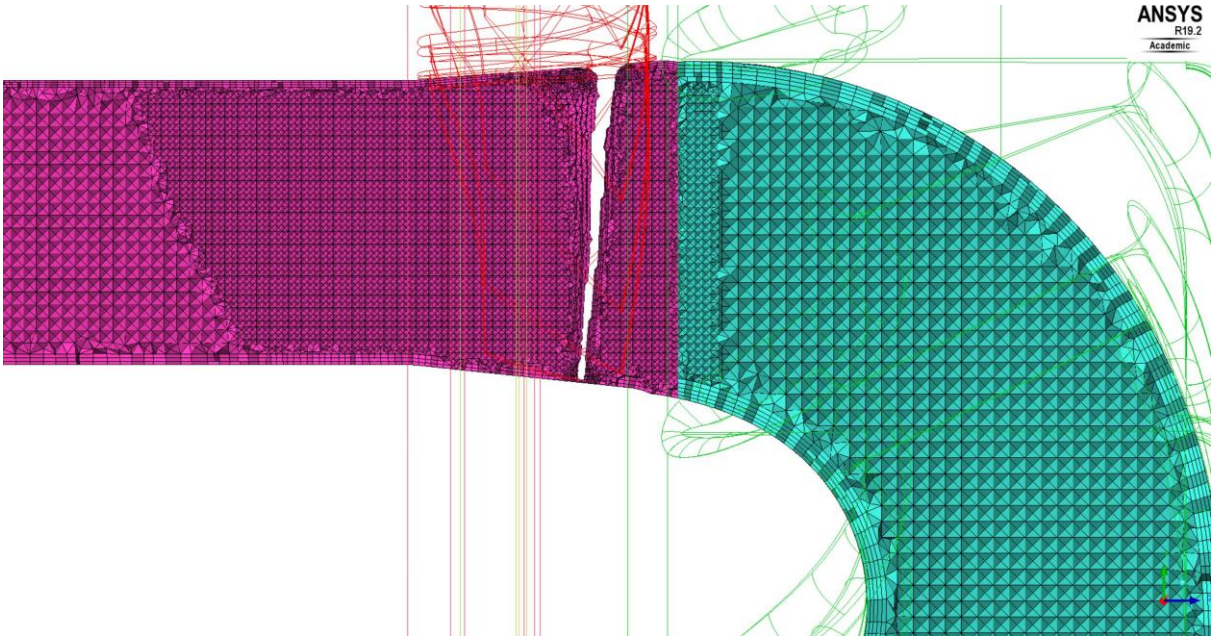

Figure C.1 – Detailed view at prism layers in blisk region and interface between stationary and rotational cell zone

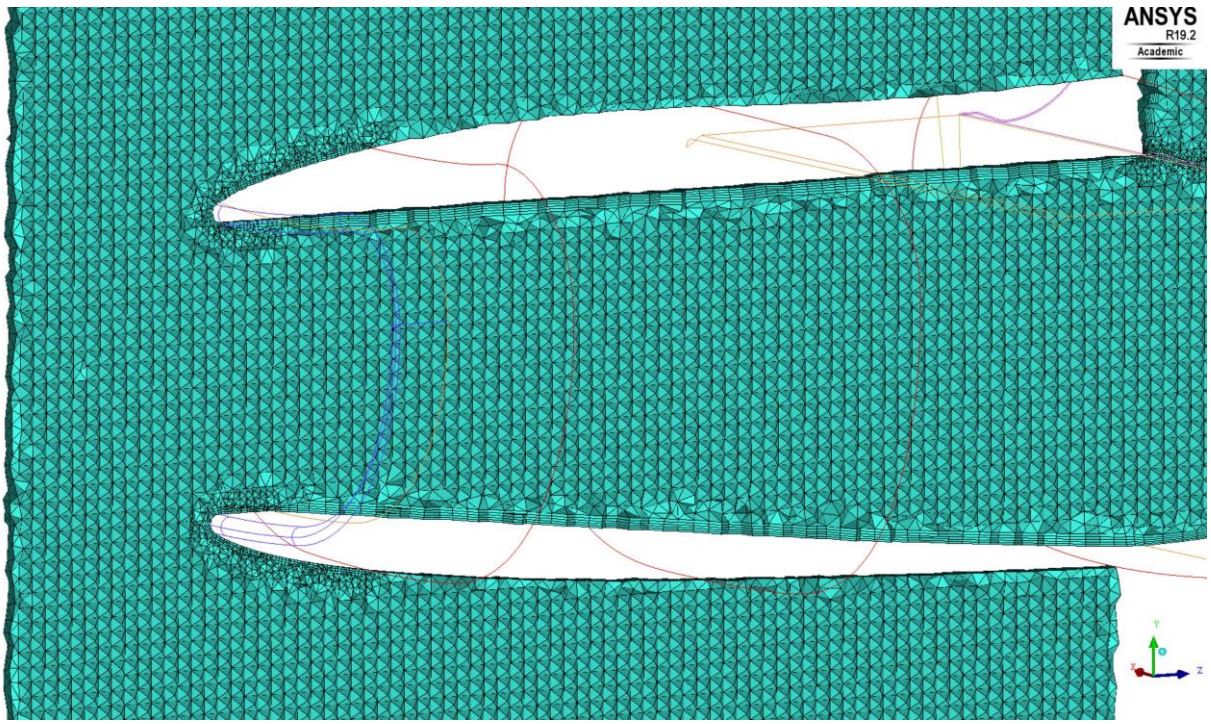

Figure C.2 – Detailed view at prism layers in diffuser region

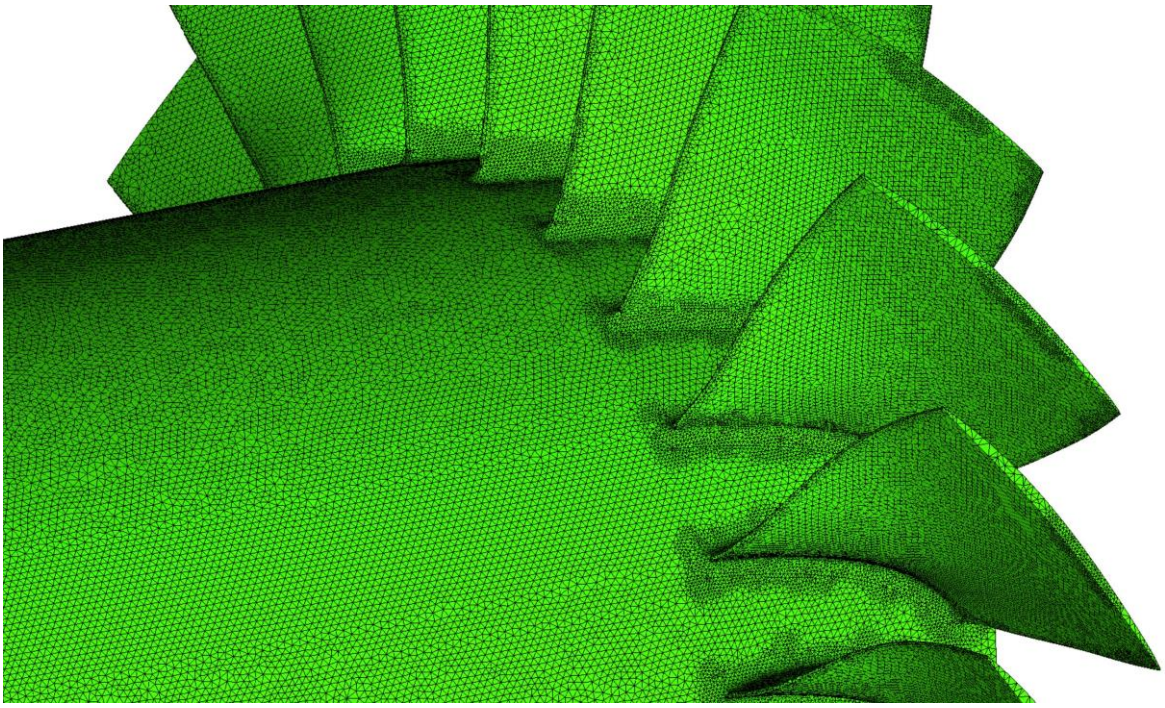

Figure C.3 – Detailed view at surface mesh of blisk, note refined section at blade tip due to proximity of shroud

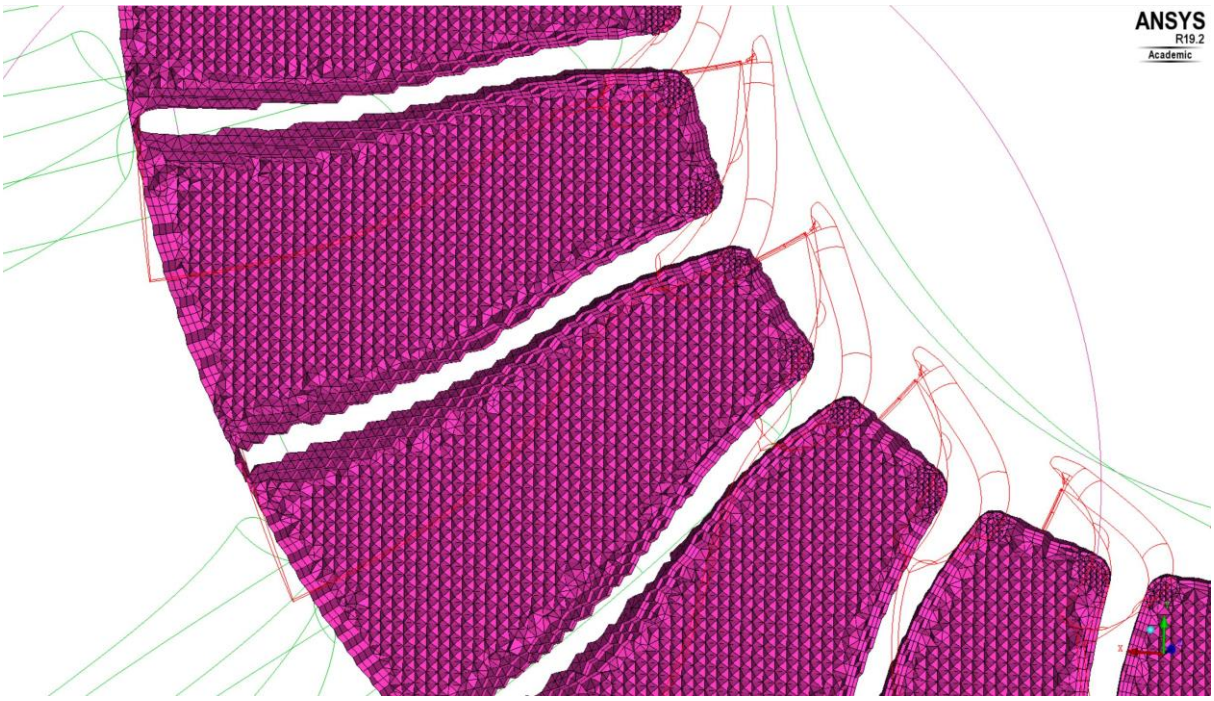

Figure C.4 – Detailed view at grid and inflation of blisk blades

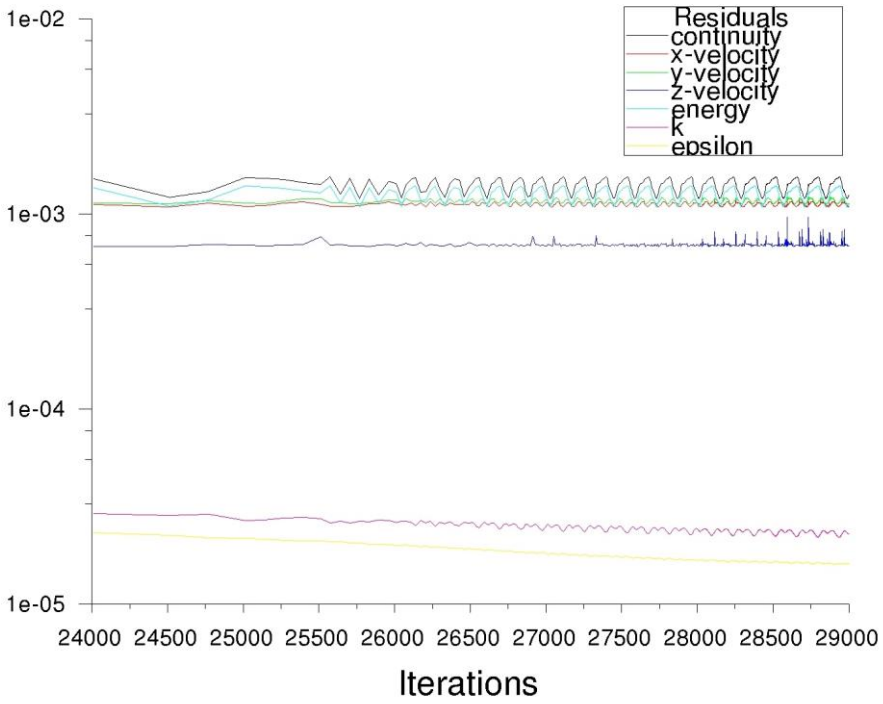

Figure C.5 – Residual levels, only last 5000 iterations are showed

The case ran for 30 thousand iterations with slightly different mesh and calculation was interpolated to final mesh and run for another 29 thousand iterations, in total therefore 60 thousand iterations.

Appendix D

Following tables contain all polynomial formulations of restitution coefficients derived by Abedi (2009).

Table D.5.1 – Polynomial formulation of normal coefficient of restitution for various impact velocities, θ_{in} is in degrees, bolded polynomials were used in IPS study, adopted from (Abedi, 2009, pp. 138-142)

impact velocity [m/s]	θ_{in}^3	θ_{in}^2	θ_{in}	-
100	-1.00E-06	0.0003	-0.0234	1.1338
50	**-1.00E-06**	**0.0003**	**-0.0219**	**1.0951**
10	**-5.00E-07**	**0.0001**	**-0.0085**	**0.9465**
5	-5.00E-07	0.0001	-0.0071	0.9637

Table D.5.2 – Polynomial formulation of tangential coefficient of restitution for various particle diameters, θ_{in} is in degrees, bolded polynomial was used in IPS study, adopted from (Abedi, 2009, pp. 138-142)

particle diameter [μm]	θ_{in}^3	θ_{in}^2	θ_{in}	-
15	-5.00E-06	0.0008	-0.0402	1.3541
50	2.00E-06	-9.00E-05	0.0008	0.6376
150	2.00E-07	-5.00E-05	0.0028	0.582
500	**-2.00E-07**	**-0.0001**	**0.0109**	**0.5867**
700	-4.00E-07	-7.00E-05	0.0072	0.6767

Appendix E

All calculated correlations to real damage are gathered and stated in following tables.

particle diameter [mm]	e = 1	e = 0.9	e = 0.8	e = 0.7	e = 0.6	e_n50e_t500	e_n10e_t50
0.3	0,741492	0,65838	0,710313	0,59354	0,634911	0,515538	0,730927
0.5	0,691094	0,753325	0,747029	0,669839	0,710398	0,566449	0,762247
1	0,689882	0,686881	0,67924	0,642675	0,63631	0,522912	0,569238
1.5	0,615346	0,64963	0,545374	0,586302	0,714619	0,476997	0,552405
2	0,526492	0,570199	0,491702	0,59129	0,612473	0,471345	0,515097
2.5	0,534572	0,560275	0,569294	0,558065	0,621456	0,558809	0,394795

particle diameter [mm]	e = 1	e = 0.9	e = 0.8	e = 0.7	e = 0.6	e_n50e_t500	e_n10e_t50
0.3	0,72434	0,682906	0,701238	0,692168	0,63109	0,590296	0,703867
0.5	0,704684	0,672938	0,659553	0,656532	0,701667	0,546292	0,691223
1	0,571479	0,630749	0,632299	0,604836	0,661781	0,511271	0,515407
1.5	0,487973	0,480608	0,508942	0,625384	0,633854	0,432082	0,45421
2	0,516329	0,538772	0,408702	0,588563	0,615938	0,435688	0,456011
2.5	0,54705	0,520939	-[1]	0,393789	0,42762	0,50896	0,563521

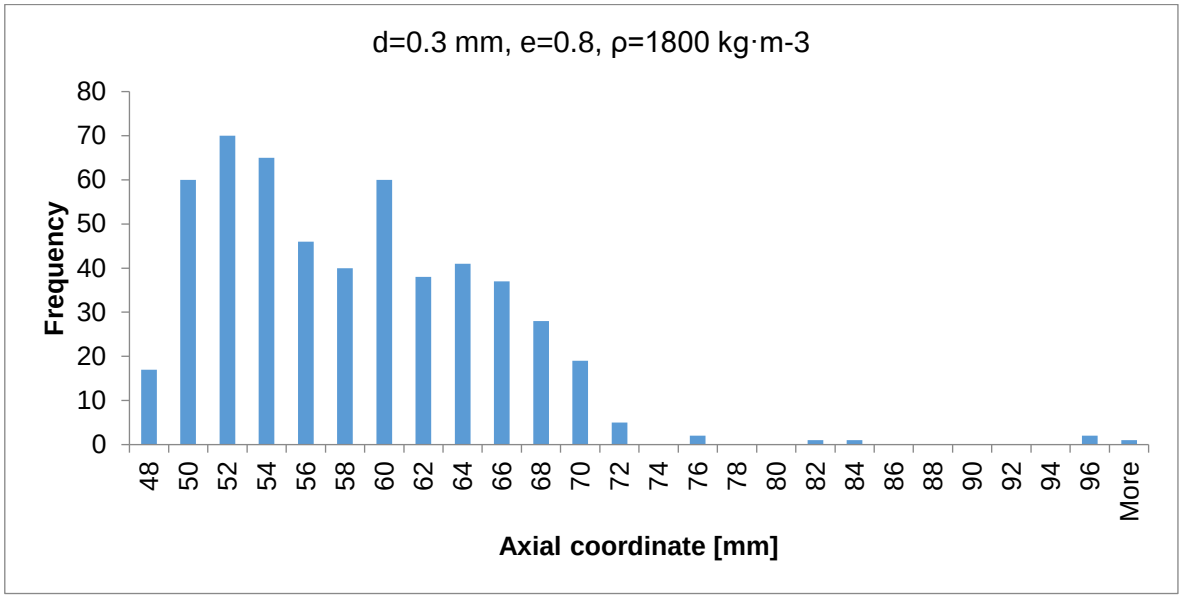

Figure E.1 – Histogram of particle impacts at rotor surface sorted by radial coordinate

[1] This result did not pass t-test for statistical significance.

Appendix F

The rest of trajectories of particles with different density, all parameters are stated in figures and thorough description is provided in chapter 4.

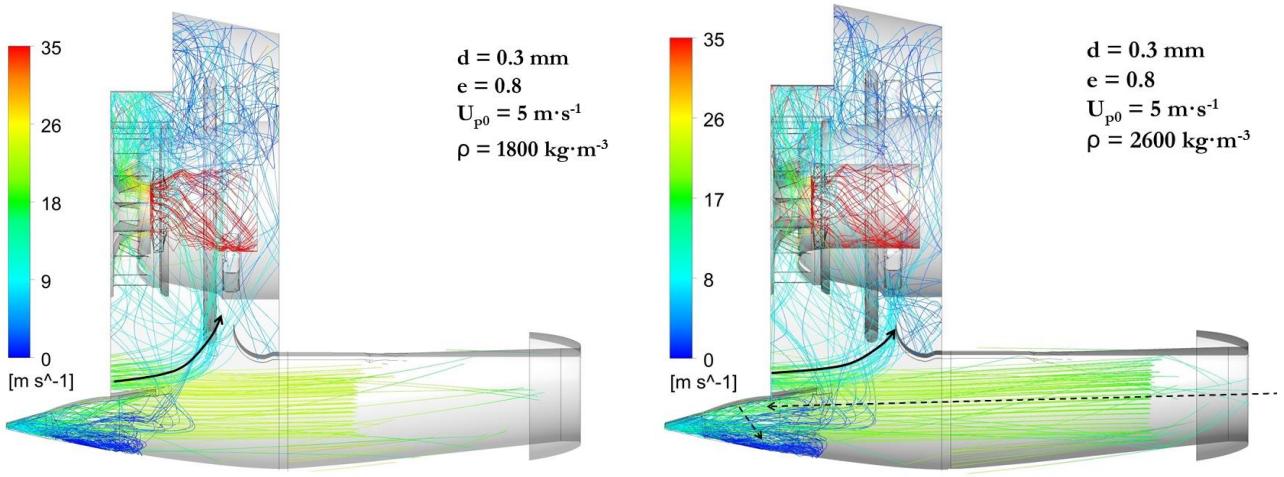

Figure F.1 – Particle trajectories with injection velocity of 5 m·s^{-1}

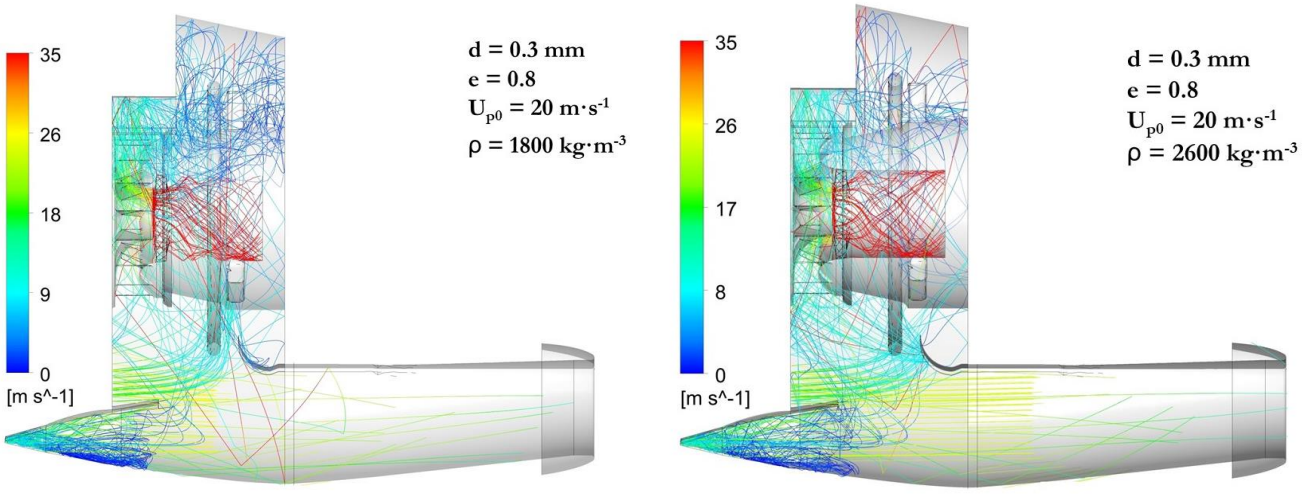

Figure F.2 - Particle trajectories with injection velocity of 20 m·s^{-1}

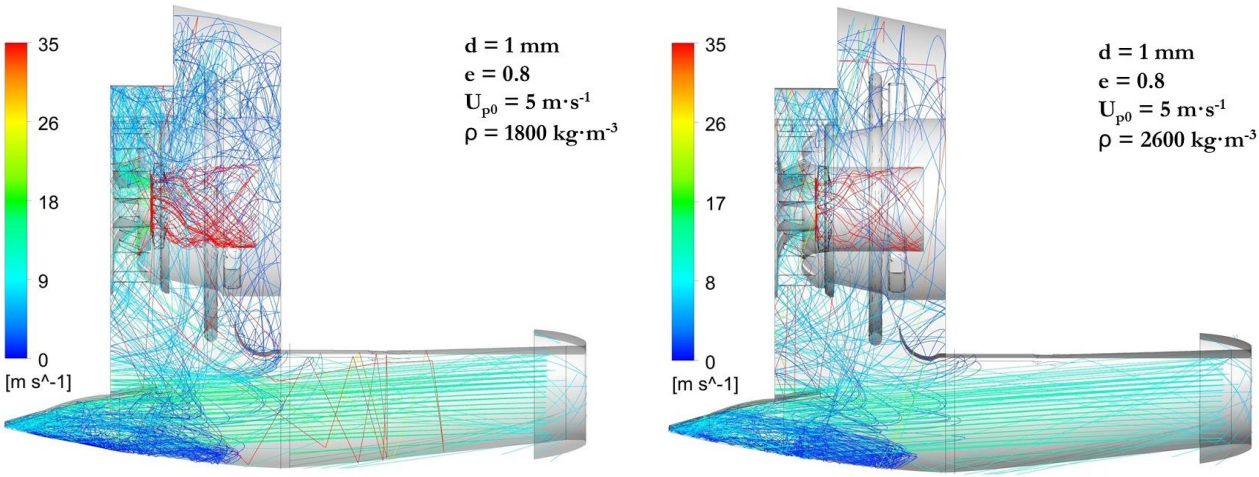

Figure F.3 - Particle trajectories with injection velocity of 5 m·s^{-1}

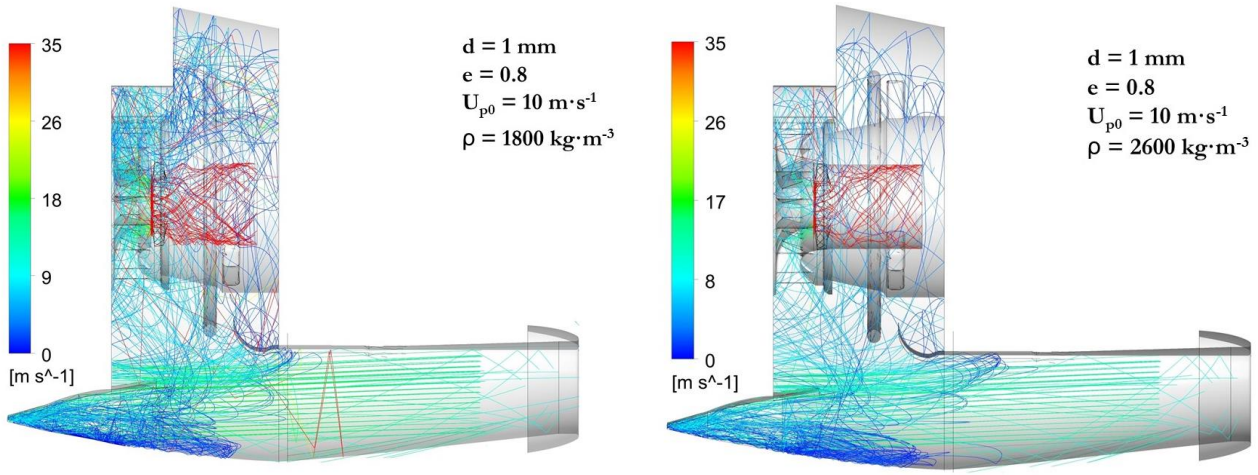

Figure F.4 - Particle trajectories with injection velocity of 10 m·s^{-1}